

On the hydraulic fracturing in naturally-layered porous media using the phase field method

Xiaoying Zhuang², Shuwei Zhou^{1,2*}, Mao Sheng³, Gengsheng Li³

1 Department of Geotechnical Engineering, College of Civil Engineering, Tongji University, Shanghai 200092, P.R. China

2 Institute of Continuum Mechanics, Leibniz University Hannover, Hannover 30167, Germany

3 State Key Laboratory of Petroleum Resources and Prospecting, China University of Petroleum, Beijing, China

* Corresponding author: Shuwei Zhou (shuwei.zhou@ikm.uni-hannover.de; zhoushuwei1016@126.com)

Abstract

In the hydraulic fracturing of natural rocks, understanding and predicting crack penetrations into the neighboring layers is crucial and relevant in terms of cost-efficiency in engineering and environmental protection. This study constitutes a phase field framework to examine hydraulic fracture propagation in naturally-layered porous media. Biot's poroelasticity theory is used to couple the displacement and flow field, while a phase field method helps characterize fracture growth behavior. Additional fracture criteria are not required and fracture propagation is governed by the equation of phase field evolution. Thus, penetration criteria are not required when hydraulic fractures reach the material interfaces. The phase field method is implemented within a staggered scheme that sequentially solves the displacement, phase field, and fluid pressure. We consider the soft-to-stiff

and the stiff-to-soft configurations, where the layer interface exhibits different inclination angles θ . Penetration, singly-deflected, and doubly-deflected fracture scenarios can be predicted by our simulations. In the soft-to-stiff configuration, $\theta = 0^\circ$ exhibits penetration or symmetrical doubly-deflected scenarios, and $\theta = 15^\circ$ exhibits singly-deflected or asymmetric doubly-deflected scenarios. Only the singly-deflected scenario is obtained for $\theta = 30^\circ$. In the stiff-to-soft configuration, only the penetration scenario is obtained with widening fractures when hydraulic fractures penetrate into the soft layer.

Keywords: Cap layer, Reservoir layer, Numerical simulation, Phase field, Hydraulic fracturing, Staggered scheme

1 Introduction

Hydraulic fracturing (HF) in porous media is a challenging area for mechanical, environmental, energy, and geological engineering (Cui et al., 2013; Guo and Fall, 2018; Jeanpert et al., 2019; Lei et al., 2017; Li et al., 2014; Liu and Sheng, 2019; Mikelic et al., 2013; Zhou et al., 2018a). On the one hand, HF applies pressurized fluid (Liu et al., 2014) to form highly permeable fractures into the rock strata and the fracture network facilitate the linking of wellbores with the expected natural resources. On the other hand, HF is also relatively controversial because of its potential impact on the engineering geological environment. Unexpected fractures may be stimulated and propagate into neighboring rock strata, thereby resulting in a risk of water contamination. Moreover, uncontrolled hydraulic fractures along dominant or previously unknown faults may cause an increase in seismic activity (Kim, 2013), which is detrimental to the stability of the entire geological system. Therefore, better prediction of hydraulic fracture propagation is one

of the most critical issues in recent years (Figueiredo et al., 2017; Liu et al., 2018; Ren et al., 2017a; Zhou et al., 2018c), especially in engineering geology.

Naturally-layered rock strata are an important and representative part of the engineering geological environment. In general, numerous natural or artificial discontinuities are contained in naturally-layered reservoirs, such as fractures or material interfaces. Many studies have examined how fluid-driven fractures interact with natural discontinuities. Some contributions can be referred to Behnia et al. (2014); Biot et al. (1983); Dahi-Taleghani et al. (2011); Dyskin and Caballero (2009); Gudmundsson and Brenner (2001); Khoei et al. (2015); Van Eekelen et al. (1982); Wang (2015); Zhang and Ghassemi (2011). These studies have indicated that three fracture patterns exist in layered domains, particular when hydraulic fractures reach the layer interfaces: penetration, singly-deflected, and doubly-deflected scenarios (see Fig. 1). However, these studies have yet to achieve a consensus on mechanisms for different fracture penetration patterns. Hence, predicting hydraulic fractures in naturally-layered media remains an open research topic and new insights should be provided to conduct further research.

For example, advanced numerical approaches can be applied in naturally-layered media, although hydraulic fractures can be also investigated either analytically (Santillán et al., 2017) or experimentally (Cooke and Underwood, 2001; Xing et al., 2018). The numerical models for fracture can be classified into discrete and continuous approaches, including the extended finite element method (XFEM) (Moës and Belytschko, 2002), cohesive element method (Nguyen et al., 2001), element-erosion method (Belytschko and Lin, 1987), phantom-node method (Rabczuk et al., 2008), mesh-free methods (Zhuang et al., 2012, 2014), cracking particle methods (Rabczuk et al., 2010), peridynamics (Ren et al., 2016, 2017b), gradient damage models (Peerlings et al., 1996), screened-Poisson models (Areias et al., 2016), and phase field models (PFMs) (Borden

et al., 2012; Miehe et al., 2010a,b; Zhou et al., 2019a). Although some continuous and discrete approaches have been used in HF, predicting fracturing networks across different rock formations, such as reservoir and cap layers, remains a challenging topic. For example, an XFEM framework (Vahab et al., 2018) was recently established to investigate hydraulic fracture propagation in a layered domain. Nevertheless, mandatory penetration criteria are applied when the fractures reach the layer interfaces. Although singly-deflected and penetration scenarios can be observed, the hydraulic fractures are “man-made”, and not the automatically predicted ones with respect to physical principles.

The current study investigates the propagation of hydraulic fractures in naturally layered geological formations by applying the phase field model (Zhou et al., 2018c) to solve the fracture penetration issue at the layer interface and provide a new perspective. Note that the used PFM is based on the quasi-static formulation of Zhou et al. (2018c) for fluid-driven fracture, which is different from the PFMs for single-phase solid (Zhou et al., 2018b,d) and for dynamic fluid-driven fracture (Zhou et al., 2019b). In the numerical investigation, we consider two configurations, namely, the soft-to-stiff and the stiff-to-soft, and also different inclination angles of the layer interface. The phase field characteristics of fluid-driven fracture in layered geological formations are firstly and systematically explored. In addition, the displacement and stress characteristics related to geological system stability are investigated. The relationship between the phase field (fracture pattern) and the stiffness contrast and inclination angle of the geological formations, is also further revealed. Based on minimization of the energy functional, our simulations automatically reveal the three potential fracture scenarios in naturally-layered geological formations, i.e., the penetration, singly-deflected, and doubly-deflected scenarios, which must be achieved by other numerical methods such as XFEM (Vahab et al., 2018) by imposing

“man-made” penetration criteria.

The phase field simulation in this study can deepen our understanding of crack patterns and their governing factors in layered geological formations. The successful application of PFM also shows its immense potential in modeling the interface crack between two layers and how cracks appear into neighboring layers, which are not easily captured with conventional methods. The remainder of this paper is organized as follows: Sections 2, 3, and 4 present the theoretical model, numerical implementation, and validation examples, respectively. Sections 5 and 6 provide the numerical investigations on the soft-to-stiff and stiff-to-soft configurations, respectively. Lastly, Section 7 concludes this study.

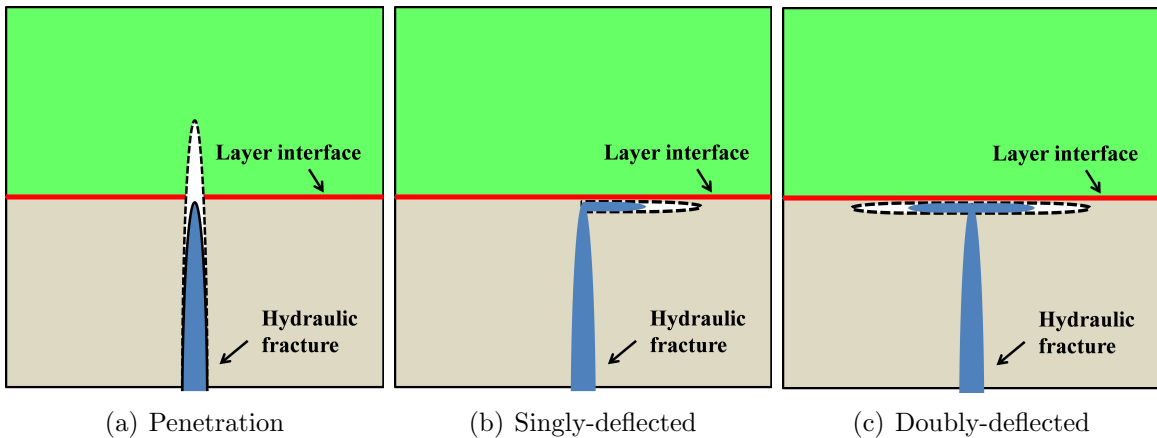


Fig. 1. Three fracture patterns when hydraulic fractures reach the layer interface (Vahab et al., 2018)

2 Mathematical models for fracture propagation

2.1 Energy functional

Let Ω be a cracked two-dimensional permeable porous solid and \mathbf{x} be the position vector in Fig.

2. Two different layers, Ω_A and Ω_B , compose the calculation domain Ω ($\Omega_A \cup \Omega_B = \Omega$). The

full bond between the two layers is assumed and continuity conditions are naturally fulfilled. The boundary of the domain Ω is $\partial\Omega$. Two disjointed parts, $\partial\Omega_u$ and $\partial\Omega_t$, are defined with the prescribed displacement $\bar{\mathbf{u}}(\mathbf{x}, t)$ and traction $\mathbf{t}^*(\mathbf{x}, t)$. Moreover, a body force $\mathbf{b}(\mathbf{x}, t)$ is applied on Ω . We also define the outward unit normal vector \mathbf{n} and the internal fracture in the domain as Γ in Fig. 2. The main purpose of this study is to investigate fracture propagation in the domains Ω_A and Ω_B , particularly the fracture behavior around the interface of the two layers. Furthermore, this research assumes that the pore size is considerably smaller than the fracture length scale; the porous media are elastic and homogeneous with compressible and viscous fluids.

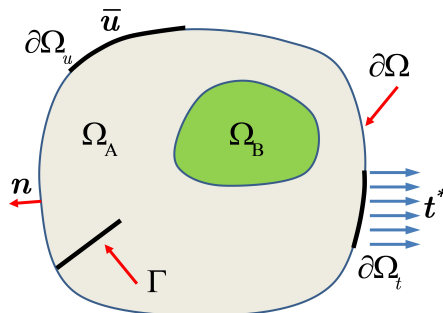


Fig. 2. Layered porous media

We use the variational approach of Griffith's theory (Francfort and Marigo, 1998) to study fracture propagation. For the purely single phase problem, the energy functional $\Psi(\mathbf{u}, \Gamma)$ for the entire calculation domain is composed of only the elastic energy $\Psi_\varepsilon(\boldsymbol{\varepsilon})$, dissipation energy Ψ_f and external work W_{ext} (Zhou et al., 2018b). By contrast, the influence of fluid pressure p must be considered in a porous medium and the energy functional involves an additional pressure-related term (Bourdin et al., 2012; Lee et al., 2016; Miehe and Mauthe, 2016; Mikelić et al.,

2015a,b; Wheeler et al., 2014; Zhou et al., 2018c):

$$\Psi(\mathbf{u}, p, \Gamma) = \underbrace{\int_{\Omega} \psi_{\varepsilon}(\boldsymbol{\varepsilon}) d\Omega}_{\Psi_{\varepsilon}} - \underbrace{\int_{\Omega} \alpha p \cdot (\nabla \cdot \mathbf{u}) d\Omega}_{\text{pressure-related term}} + \underbrace{\int_{\Gamma} G_c dS}_{\Psi_f} - \underbrace{\int_{\Omega} \mathbf{b} \cdot \mathbf{u} d\Omega - \int_{\partial\Omega_t} \mathbf{t}^* \cdot \mathbf{u} dS}_{W_{ext}} \quad (1)$$

where α and G_c represent the Biot coefficient and critical energy release rate, respectively, and $\boldsymbol{\varepsilon}$ represents the linear strain tensor.

In Eq. (1), $\psi_{\varepsilon}(\boldsymbol{\varepsilon})$ denotes the elastic energy density, which can be expressed as follows in an intact isotropic and linear elastic solid (Miehe et al., 2010a):

$$\psi_{\varepsilon}(\boldsymbol{\varepsilon}) = \frac{1}{2} \lambda \varepsilon_{ii} \varepsilon_{jj} + \mu \varepsilon_{ij} \varepsilon_{ij} \quad (2)$$

where $\lambda, \mu > 0$ are the Lamé constants.

2.2 Phase field description

The phase field model (Zhou et al., 2018c), which smears the discontinuous fracture Γ over the domain Ω , is used to describe fracture propagation in the porous media. In this study, the phase field varies from 0 to 1, $\phi = 0$ means that the material is unbroken, and $\phi = 1$ is for a “fully” broken region. Note that the value of the phase field can be used in identifying a fracture, while a damaged region bounded by a threshold value of phase field is commonly adopted to reflect the fracture shape similar to those in the discrete settings (Borden et al., 2012). Thereafter, the crack surface density is represented by the phase field and its gradient as follows (Bourdin et al., 2000):

$$\gamma(\phi, \nabla\phi) = \frac{\phi^2}{2l_0} + \frac{l_0}{2} \nabla\phi \cdot \nabla\phi \quad (3)$$

where l_0 is the length scale parameter.

The regularized formulation (3) facilitate the transfer of the dissipation energy integration over a discontinuity into an integration over a continuous domain. This treatment considerably facilitates the numerical implementation in fracture problems. Therefore, substituting Eq. (3) into Eq. (1) yields the dissipation energy Ψ_f :

$$\int_{\Gamma} G_c dS = G_c \int_{\Gamma} dS \approx G_c \int_{\Omega} \gamma d\Omega = \int_{\Omega} G_c \left[\frac{\phi^2}{2l_0} + \frac{l_0}{2} \nabla \phi \cdot \nabla \phi \right] d\Omega \quad (4)$$

In the PFM, the elastic energy appears as a driving term in the evolution equation. Therefore, for the purpose of removing unrealistic fracture patterns in the simulation (Miehe et al., 2010a), the elastic energy must be decomposed. The strain decomposition is used first where the strain $\boldsymbol{\varepsilon}$ is composed of the tensile strain tensor $\boldsymbol{\varepsilon}^+$ and compressive $\boldsymbol{\varepsilon}^-$:

$$\boldsymbol{\varepsilon}^{\pm} = \sum_{a=1}^d \langle \varepsilon_a \rangle^{\pm} \mathbf{n}_a \otimes \mathbf{n}_a \quad (5)$$

where ε_a denotes the principal strains, and \mathbf{n}_a represents the direction vectors. The two operators in Eq. (5) are $\langle \cdot \rangle^+ = \max(\cdot, 0)$ and $\langle \cdot \rangle^- = \min(\cdot, 0)$. Thereafter, the positive and negative elastic energy densities can be defined in terms of the tensile and compressive strain tensors:

$$\psi_{\boldsymbol{\varepsilon}}^{\pm}(\boldsymbol{\varepsilon}) = \frac{\lambda}{2} \langle tr(\boldsymbol{\varepsilon}) \rangle^{\pm 2} + \mu tr(\boldsymbol{\varepsilon}^{\pm 2}) \quad (6)$$

According to Miehe et al. (2010a), the total elastic energy density is expressed as

$$\psi_{\boldsymbol{\varepsilon}}(\boldsymbol{\varepsilon}) = [(1 - k)(1 - \phi)^2 + k] \psi_{\boldsymbol{\varepsilon}}^+(\boldsymbol{\varepsilon}) + \psi_{\boldsymbol{\varepsilon}}^-(\boldsymbol{\varepsilon}) \quad (7)$$

where $0 < k \ll 1$ is a stability parameter. In Eq. (7), if the phase field $\phi = 1$, then the stiffness against tension is only k times of its original value, and $k = 0$ will lead to a singularity in the stiffness matrix. Therefore, the positive stability parameter can effectively avoid this singularity and its detrimental effect on convergence in the simulation.

2.3 Governing equations for the phase field evolution

The energy functional (1) is renewed according to Eqs. (4) and (7). For the variational approach (Francfort and Marigo, 1998), fracture initiation and growth at time t is a process that the energy functional Ψ seeks for a minimum value. In a natural manner, setting the first variation of the functional Ψ as 0 yields

$$\delta\Psi = \underbrace{\int_{\partial\Omega_t} [(\sigma_{ij} - \alpha p \delta_{ij}) n_j - t_i^*] \delta u_i dS}_{\textcircled{1}} - \underbrace{\int_{\Omega} [(\sigma_{ij} - \alpha p \delta_{ij})_{,j} + b_i] \delta u_i d\Omega}_{\textcircled{2}} - \underbrace{\int_{\Omega} \left[2(\phi - 1)(1 - k)\psi_{\varepsilon}^+ + \frac{G_c \phi}{l_0} - G_c l_0 \frac{\partial^2 \phi}{\partial x_i^2} \right] \delta \phi d\Omega}_{\textcircled{3}} + \underbrace{\int_{\partial\Omega} \left(\frac{\partial \phi}{\partial x_i} n_i \right) \delta \phi dS}_{\textcircled{4}} = 0 \quad (8)$$

where the component of the effective stress tensor $\boldsymbol{\sigma}(\boldsymbol{\varepsilon})$ is

$$\sigma_{ij} = [(1 - k)(1 - \phi)^2 + k] \frac{\partial \psi_{\varepsilon}^+}{\partial \varepsilon_{ij}} + \frac{\partial \psi_{\varepsilon}^-}{\partial \varepsilon_{ij}} \quad (9)$$

Thereafter, the Cauchy stress tensor $\boldsymbol{\sigma}^{por}$ (Lee et al., 2016) is set as follows:

$$\boldsymbol{\sigma}^{por}(\boldsymbol{\varepsilon}) = \boldsymbol{\sigma}(\boldsymbol{\varepsilon}) - \alpha p \mathbf{I}, \quad in \Omega \quad (10)$$

In Eq. (10), the dimensionless Biot coefficient α reflects the extent of perturbation in the total stress $\boldsymbol{\sigma}^{por}$ owing to the changes in fluid pressure p (Segall and Fitzgerald, 1998). Given that Eq. (8) consistently holds for all possible $\delta \mathbf{u}$ and $\delta \phi$, in Eq. (8)② and ③, except the displacement and phase field variations, the main bodies in the integrals must constantly be 0. Therefore, Eq. (8)② and ③ produce the following governing equations:

$$\left\{ \begin{array}{l} \frac{\partial \sigma_{ij}^{por}}{\partial x_j} + b_i = 0 \\ \left[\frac{2l_0(1-k)\psi_\varepsilon^+}{G_c} + 1 \right] \phi - l_0^2 \frac{\partial^2 \phi}{\partial x_i^2} = \frac{2l_0(1-k)\psi_\varepsilon^+}{G_c} \end{array} \right. \quad (11)$$

To ensure the availability of PFM, the irreversibility condition must be established which indicates that a fracture cannot be healed. An easy treatment is the introduction of a history field $H(\mathbf{x}, t)$, which represents the maximum tensile elastic energy density at the time interval $[0, t]$ (Borden et al., 2012; Miehe et al., 2010a,b). That is, the history field H can be expressed as follows:

$$H(\mathbf{x}, t) = \max_{s \in [0, t]} \psi_\varepsilon^+(\boldsymbol{\varepsilon}(\mathbf{x}, s)) \quad (12)$$

History field H satisfies the Kuhn-Tucker conditions (Miehe et al., 2010a). Thereby, a monotonic increase in the phase field is ensured under compression or unloading. Substituting $H(\mathbf{x}, t)$ into ψ_ε^+ , Eq. (11) yields the following strong form:

$$\left\{ \begin{array}{l} \frac{\partial \sigma_{ij}^{por}}{\partial x_i} + b_i = 0 \\ \left[\frac{2l_0(1-k)H}{G_c} + 1 \right] \phi - l_0^2 \frac{\partial^2 \phi}{\partial x_i^2} = \frac{2l_0(1-k)H}{G_c} \end{array} \right. \quad (13)$$

Apart from the Dirichlet boundary condition, Eq. (13) is also subjected to the Neumann

condition:

$$\sigma_{ij}^{por} n_j = t_i, \quad \text{on } \partial\Omega_t \quad (14)$$

In addition, the entire calculation domain has an initial phase field $\phi_0 = 0$ and the approach of [Borden et al. \(2012\)](#) is used to artificially induce a pre-existing crack.

2.4 Flow field

Three parts of the flow domain are distinguished: unbroken domain (reservoir domain) $\Omega_r(t)$, fracture domain $\Omega_f(t)$, and transition domain $\Omega_t(t)$ ([Zhou et al., 2018c](#)). These three domains are defined by setting two phase field thresholds, c_1 and c_2 . The subdomain is an unbroken domain $\Omega_r(t)$ if $\phi \leq c_1$, but a fracture domain $\Omega_f(t)$ if $\phi \geq c_2$. In the case of $c_1 < \phi < c_2$, the subdomain is a transition domain. Given that a sharp fracture is diffused in PFM, determining the hydraulic and solid parameters in the transition domain is evidently a challenge. For simplicity, many studies such as [Lee et al. \(2016, 2017a,b\)](#); [Mikelić et al. \(2015a\)](#); [Zhou et al. \(2018c\)](#) have adopted linear interpolation between the unbroken and fractured domains for the flow field, which was proven to receive favorable numerical results. The current study uses a linear relationship between the hydraulic and solid parameters of the unbroken and fractured domains. Thereafter, two indicator functions, χ_r and χ_f , are naturally established by applying the phase field ϕ ([Lee et al., 2016](#)):

$$\chi_r(\cdot, \phi) = \begin{cases} 1, & \phi \leq c_1 \\ \frac{c_2 - \phi}{c_2 - c_1} & c_1 < \phi < c_2, \\ 0, & \phi \geq c_2 \end{cases}, \quad \chi_f(\cdot, \phi) = \begin{cases} 0, & \phi \leq c_1 \\ \frac{\phi - c_1}{c_2 - c_1} & c_1 < \phi < c_2 \\ 1, & \phi \geq c_2 \end{cases} \quad (15)$$

Note that the indicator functions χ_r and χ_f have also been established in [Lee et al. \(2016, 2017a,b\)](#); [Mikelić et al. \(2015a\)](#); [Zhou et al. \(2018c\)](#), indicating that the fracture pattern is relatively insensitive to the indicator functions. In addition, [Lee et al. \(2016\)](#) suggested a relation $c_1 = 0.5 - m_x$ and $c_2 = 0.5 + m_x$, with $0 < m_x < 0.5$. However, this study considers c_1 and c_2 as two independent values.

Darcy's law is applied to describe the flow field in the porous media. In the entire domain, mass conservation is expressed as follows([Zhou et al., 2018c](#)):

$$\rho S \frac{\partial p}{\partial t} + \nabla \cdot (\rho \mathbf{v}) = q_m - \rho \alpha \chi_r \frac{\partial \varepsilon_{vol}}{\partial t} \quad (16)$$

where ρ , S , \mathbf{v} , and ε_{vol} are the flow density, storage coefficient, flow velocity, volumetric strain of the domain, and source term, respectively. By denoting ρ_r and ρ_f as the fluid densities in Ω_r and Ω_f , we have $\rho = \rho_r \chi_r + \rho_f \chi_f$; similarly, $\alpha = \alpha_r \chi_r + \alpha_f \chi_f$. Given that the Biot coefficient $\alpha = 1$ for the fracture domain, $\alpha = \alpha_r \chi_r + \chi_f$, with α_r representing the Biot coefficient in Ω_r . In addition, the volumetric strain $\varepsilon_{vol} = \nabla \cdot \mathbf{u}$. Note that we provide one feasible model for coupling the fluid flow with the phase field. We mention that more general methods such as the one proposed by [Pudasaini \(2016\)](#) can be applied to provide improved description of the fluid flow through the porous media.

The storage coefficient S can be expressed as follows ([Zhou et al., 2018c](#)):

$$S = \varepsilon_p c + \frac{(\alpha - \varepsilon_p)(1 - \alpha)}{K_{Vr}} \quad (17)$$

where ε_p , c , and K_{Vr} are the porosity, fluid compressibility, and bulk modulus of Ω_r , respectively.

Naturally, $c = c_r\chi_r + c_f\chi_f$, with c_r and c_f as the respective fluid compressibility in Ω_r and Ω_f . Note that we set $\varepsilon_p = 1$ for Ω_f . Therefore, $\varepsilon_p = \varepsilon_{pr}\chi_r + \chi_f$, with ε_{pr} representing the porosity of the reservoir domain.

Darcy's velocity \mathbf{v} is subsequently expressed as

$$\mathbf{v} = -\frac{K}{\mu_e}(\nabla p + \rho\mathbf{g}) \quad (18)$$

where K and μ_e represent the effective permeability and fluid viscosity, respectively. $K = K_r\chi_r + K_f\chi_f$, with K_r and K_f being the permeabilities of Ω_r and Ω_f , respectively. $\mu_e = \mu_r\chi_r + \mu_f\chi_f$, while μ_r and μ_f are the fluid viscosity in Ω_r and Ω_f , respectively; \mathbf{g} denotes the gravity. Moreover, the novel method proposed by Pudasaini (2016) can extensively describe the fluid flow velocity in porous media. The feasibility and advantages of this method in the phase field modeling will be examined in future research.

Lastly, the following equation that governs fluid flow in Ω is expressed in terms of p :

$$\rho S \frac{\partial p}{\partial t} - \nabla \cdot \frac{\rho K}{\mu_e}(\nabla p + \rho\mathbf{g}) = q_m - \rho\alpha\chi_r \frac{\partial \varepsilon_{vol}}{\partial t} \quad (19)$$

which is subjected to the Dirichlet and Neumann conditions as shown in Zhou et al. (2018c).

3 Numerical implementation

Finite element method (FEM) is used to solve the governing equations of the multi-field fracture problem in the porous media. Therefore, weak-form formulations are required (Zhou et al., 2018c) with a modified stiffness matrix to solve the displacement field. The implicit Generalized-

α method (Borden et al., 2012) is used to discretize the time domain and unconditionally enhance numerical stability. In addition, we subsequently solve the three fields in a staggered manner. That is, solving each field is independent in one time step. Note that we couple \mathbf{u} and p and solve them in one staggered step. Table 1 presents the flowchart of the staggered scheme for the hydraulic fracture propagation in naturally-layered porous media. The Newton-Raphson iteration method is used (Zhou et al., 2018c, 2019b) in each segregated step.

Table 1: Solution flowchart for fracture propagation in the naturally-layered porous media

Initiation
$\mathbf{u}_0, \phi_0, H_0, p_0$
For every successive time step $n + 1$ do
$\mathbf{u}_n, \phi_n, H_n,$ and p_n are known
Initiation
Construct the initial guess $(\mathbf{u}, p)_{n+1}^{j=0}, H_{n+1}^{j=0},$ and $\phi_{n+1}^{j=0}$
For every successive iteration step $j + 1$ do
$(\mathbf{u}, p)_n^j, H_n^j,$ and ϕ_n^j are known
1. Solve $(\mathbf{u}, p)_{n+1}^{j+1}$ by using $(\mathbf{u}, p)_{n+1}^j, H_{n+1}^j,$ and ϕ_{n+1}^j
2. Update H_{n+1}^{j+1} by using $(\mathbf{u}, p)_{n+1}^j$ and H_{n+1}^j
3. Solve ϕ_{n+1}^{j+1} by using $(\mathbf{u}, p)_{n+1}^{j+1}, H_{n+1}^{j+1},$ and ϕ_{n+1}^j
4. Evaluate the global relative error of (\mathbf{u}, p, H, ϕ)
until the tolerance $< \varepsilon_t = 1 \times 10^{-4}$
End

4 Validation of PFM for hydraulic fracture

The fluid-driven fracture in a permeable solid is affected by competing dissipative processes owing to fluid viscosity and medium toughness (Detournay, 2016). Therefore, we check the fracture propagation and fluid pressure in the following cases (Santillán et al., 2017) to further validate the used phase field method:

- Toughness-dominated regime. The porous medium is impermeable and fracturing expends

substantially higher energy than the viscous dissipation.

- Viscous-dominated regime. The porous medium is impermeable and energy dissipation in fracture propagation is considerably lower than the viscous dissipation.
- Leak-off toughness-dominated regime. The porous medium is permeable and more fluid is stored in the porous medium than in the fracture. In addition, fracturing expends significantly higher energy than the viscous dissipation.

A $60 \text{ m} \times 30 \text{ m}$ rectangular domain is considered with an initial injection notch of $1.2 \text{ m} \times 0.2 \text{ m}$ in the domain center. After being modeled through the initial history field, the initial notch has a fluid injection rate of Q_f . All the outer boundaries of the domain are permeable with $p = 0$ and fixed in the displacement. The parameters listed in Tables 2 and 3 are used in the simulation. Note that these parameters correspond to those used in Santillán et al. (2017) for different fluid regimes.

Table 2: Basic parameters for the validation example

μ	4.722 GPa	λ	7.083 GPa	G_c	120 N/m	k	1×10^{-9}
l_0	0.4 m	c_1	0.4	c_2	1.0	ε_{pr}	0.088
ρ_r, ρ_f	$1.0 \times 10^3 \text{ kg/m}^3$	α_r	0.088	q_r	0	K_r	$1 \times 10^{-15} \text{ m}^2$
K_f	$5 \times 10^{-8} \text{ m}^2$	c_r	$1 \times 10^{-8} \text{ 1/Pa}$	c_f	$1 \times 10^{-8} \text{ 1/Pa}$	μ_r	$1 \times 10^{-3} \text{ Pa}\cdot\text{s}$

Table 3: Parameters in the toughness-dominated, viscous-dominated, and leak-off toughness-dominated regimes

Toughness dominated	Viscous dominated	Leak-off toughness dominated
Leak-off term is ignored	Leak-off term is ignored	Leak-off term is included
Q_f $10^{-3} \text{ m}^2/\text{s}$	Q_f $2 \times 10^{-4} \text{ m}^2/\text{s}$	Q_f $10^{-2} \text{ m}^2/\text{s}$
μ_f $1 \times 10^{-6} \text{ Pa}\cdot\text{s}$	μ_f $0.1 \text{ Pa}\cdot\text{s}$	μ_f $1 \times 10^{-6} \text{ Pa}\cdot\text{s}$

We discretize the domain with uniform quadrilateral elements with the maximum element size of $h = 0.2 \text{ m}$. In all simulations, a time increment $\Delta t = 0.025 \text{ s}$ is used. Figures 3 and 4

show the evolution of half-length of the fracture and fluid pressure at the fracture center for the toughness-dominated, viscous-dominated, and leak-off dominated regimes. The two figures also compare the results obtained by PFM and those by using the analytical approach presented by [Santillán et al. \(2017\)](#). Figures. 3 and 4 show that compared with the analytical method, the used PFM reproduces consistent trends in the evolution of the half-length of the fracture and mid-point fluid pressure.

Multiple reasons account for the differences in the actual values obtained by both methods. First, the used PFM aims for a permeable porous medium, whereas the analytical approach of [Santillán et al. \(2017\)](#) is for an impermeable medium. Despite using parameters that approximate an impermeable solid, this important difference cannot be completely eliminated in our phase field simulation owing to the inevitable fluid penetration. Second, the fracture in the phase field simulation evolves from an initial notch with a length of 1.2 m. Therefore, the half-length of the fracture starts from 0.6 m, and an evident ascending stage is observed before the fracture initiation in the fluid pressure-time curves. However, the analytical method assumes point-injection fluid and the initial fracture length is 0, while the increase stage before fracture initiation is disregarded. Moreover, the used PFM and analytical method include different flow models. Especially, for the leak-off toughness-dominated regime, the leak-off term in PFM is related to the volumetric strain of the domain while a fixed leak-off coefficient of $5 \times 10^{-4} \text{ m/s}^{1/2}$ is used in the analytical method according to [Santillán et al. \(2017\)](#). Another reason is that PFM smears the fracture in a finite width, while the analytical method deals with the fracture in a discrete setting.

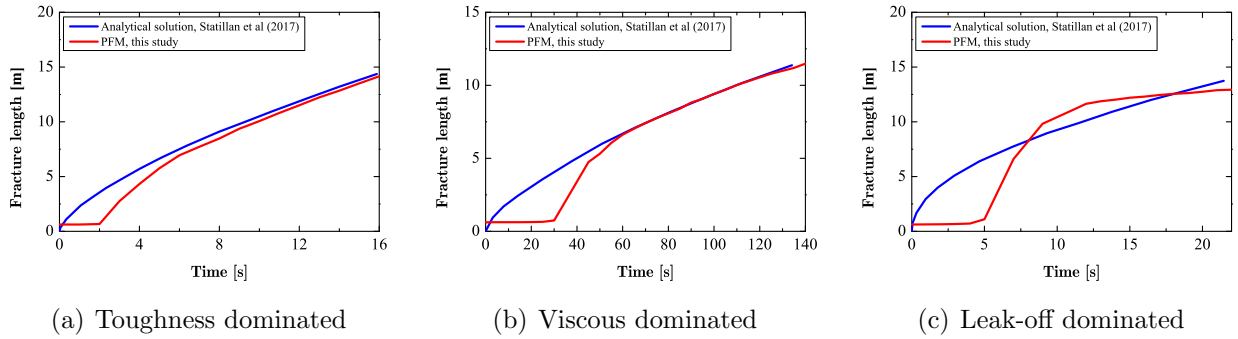


Fig. 3. Evolution of half-length of the fracture

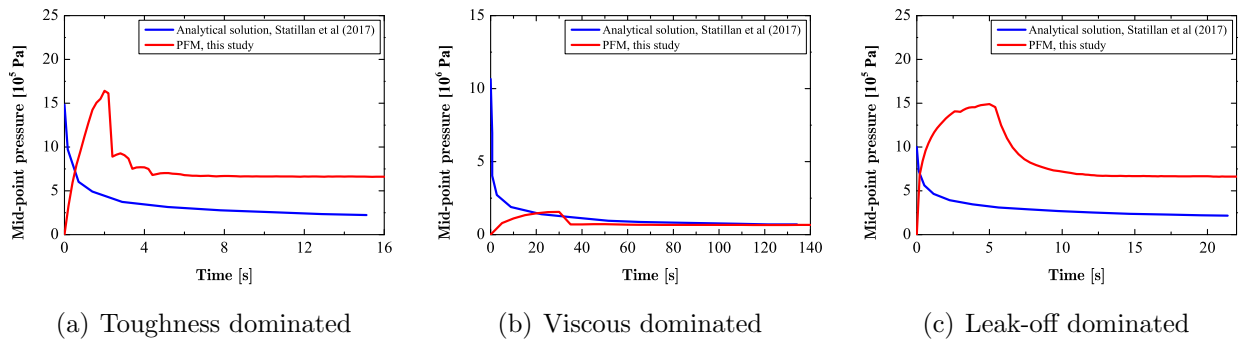


Fig. 4. Evolution of fluid pressure at the center of the fracture

5 Soft-to-stiff configuration

5.1 Geometry and boundary conditions

We investigate the hydraulic fracture pattern in two porous layers, which is a relatively typical setting in engineering geology, rock engineering, and oil/gas exploration. The setup for the two-media problem is described in Fig. 5; the center of the analysis domain is set as the origin of the coordinate system. 2D simulations are performed and we mark the two layers with the notes, ① and ②, respectively. A pre-existing notch is set in the layer ①, with its position and length also shown in Fig. 5. The width of the pre-existing notch is l_0 , while the fluid is injected into the notch with the source term $q_f = 10 \text{ kg}/(\text{m}^3 \cdot \text{s})$. Except the boundary conditions in Fig. 5, the left boundary of the layer ① is impermeable. The interface of the two layers has an inclination angle of θ . We also test the influence of the inclination angle and choose $\theta = 0^\circ, 15^\circ, \text{ and } 30^\circ$. Note that although our simulations are performed in a relative small scale that corresponds to the XFEM simulations of Vahab et al. (2018), the phase field simulation can be easily extended to large-scale problem by adjusting the geometry, mesh size, and other relevant parameters.

A total of twelve cases are examined using the various values of Young's modulus and G_c listed in Table 4. The Young's modulus E and G_c of the two layers are denoted as E_1, E_2, G_{c1} , and G_{c2} . Note that a stiffer layer exhibits a larger E and G_c than the softer layer. The Poisson's ratios of the two layers are the same (i.e., $\nu_1 = \nu_2 = 0.3$). The parameter setting in this paper is similar to that of Vahab et al. (2018) where fracture toughness k_I is used but G_c is used in the PFM. Note that the selection of the different values of Young's modulus and critical energy release rate will not affect the fracture patterns in layered domain which are depicted in Fig. 1. The other parameters of the two layers for calculation are listed in Table 5. It is quite often the

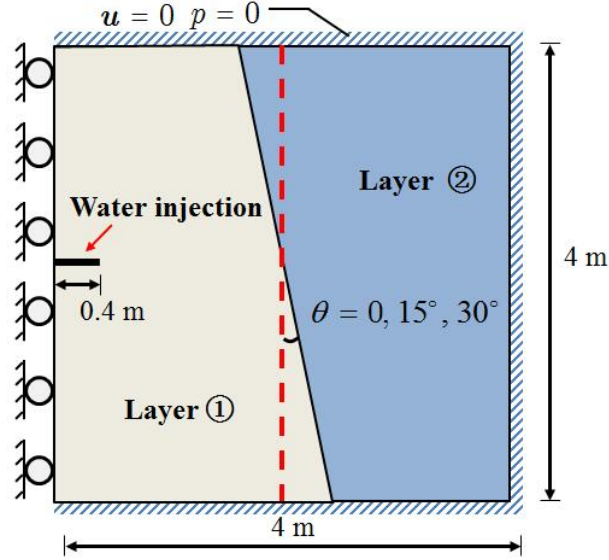


Fig. 5. Geometry and boundary conditions of the hydraulic fracture propagation in two porous layers

case in substantial rock formation the contrast of Young's modulus and tensile strength between soft and hard layers can be few times such as the pseudo fracture studies in [Gu and Siebrits \(2006\)](#). Therefore, the following cases with various combinations of material parameters for soft and hard layers relatively represent classic situations such as contract about 3 times in Young's modulus were used in [Smith et al. \(2001\)](#).

Table 4: Young's modulus and G_c of the two layers

Case number	Relationship	E_1 / GPa	E_2 / GPa	G_{c1} / (N/m)	G_{c2} / (N/m)	θ /°
1						0
2	$E_2/E_1 = 2$	60	120	2400	4800	15
3						30
4						0
5	$E_2/E_1 = 4$	30	120	1200	4800	15
6						30
7						0
8	$E_2/E_1 = 1/2$	120	60	4800	2400	15
9						30
10						0
11	$E_2/E_1 = 1/3$	120	40	4800	1600	15
12						30

Table 5: Parameters for the two layers

l_0	4×10^{-3} m	α_r	0.002	ρ_r	1.0×10^3 kg/m ³	k	1×10^{-9}
c_1	0.4	c_2	1.0	ε_{pr}	0.002	ρ_f	1.0×10^3 kg/m ³
q_r	0	q_f	0	K_r	1×10^{-15} m ²	K_f	1.333×10^{-6} m ²
c_r	1×10^{-8} 1/Pa	c_f	1×10^{-8} 1/Pa	μ_r	1×10^{-3} Pa·s	μ_f	1×10^{-3} Pa·s

The computation is performed based on the finite element meshes shown in Fig. 6. In most of the domain we use linear triangular elements that have a maximum size $h = 8$ mm. In addition, we restrict the mesh size in the region where fractures may initiate and propagate to $h = 2$ mm. The pre-existing notch is established through the initial history field H_0 and the notch width is fixed as 4 mm. In the simulation, a time step $\Delta t = 0.05$ s is used.

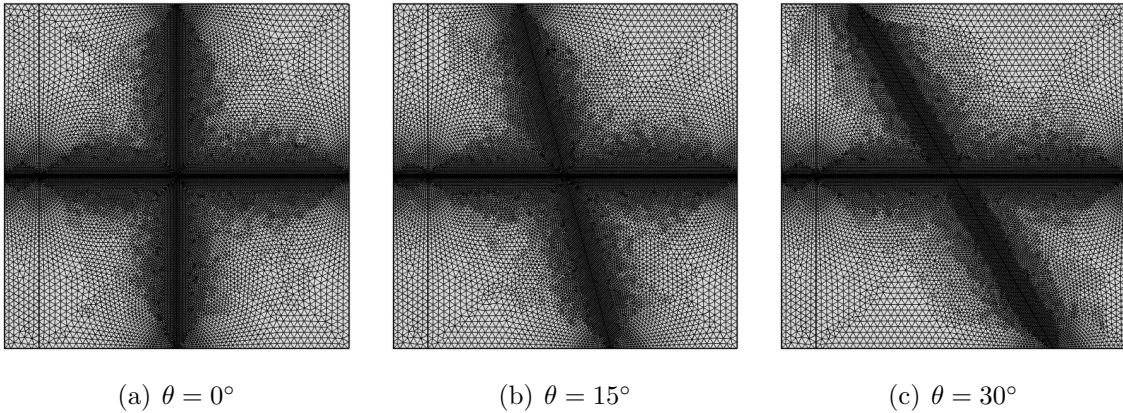


Fig. 6. Meshes for calculation

5.2 Fracture pattern

The settings of the numerical model are classified into two types, namely, soft-to-stiff configuration (Cases 1 to 6) and stiff-to-soft configuration (Cases 7 to 12). Note again that only 2D simulations are performed because 3D cases are time-consuming and unsuitable for analysis on multiple influencing factors. In addition, gravity is disregarded for simplicity, while x - and y -

axes correspond to the horizontal and vertical directions, respectively.

Figure 7 depicts the hydraulic fracture patterns for $E_2 = 2E_1$ at $t = 200$ s, in which the fractures completely propagate and their paths are evident. When the inclination angle $\theta = 0^\circ$, the penetration scenario is shown. The fracture propagates perpendicular to the interface between two layers of rock and penetrates deep into the layer ②. The reason is that the stiffness of the layer ② is insufficiently large to depress the fracture across the layer interface. The increasing fluid pressure increases the tensile stress around the fracture tip. Thereafter, the effective stress becomes higher than the tensile strength depending on the Young's modulus, fracture toughness, and length scale in the stiffer layer at the layer interface according to Zhou et al. (2018d). Therefore, the fracture cannot be prevented.

A singly-deflected scenario is observed when the inclination angle $\theta = 15^\circ$ and 30° . At an inclination angle, the fracture propagation is blocked when it reaches the layer interface. The fracture is arrested by the interface and then propagates along the interface towards the bottom boundary of the domain because of the increasing fluid injection. The singly-deflected scenario results from the fact that the fluid pressure-induced stress rotates at the layer interface in a complex manner. In this case, the decomposed effective stress exceeds the tensile strength along the interface more easily than that in the second layer.

Figure 8 presents the hydraulic fracture patterns for $E_2 = 4E_1$ at different times. When $E_2 = 4E_1$, the fracture patterns are not the same as those for $E_2 = 2E_1$. The doubly-deflected scenario is observed when $\theta = 0^\circ$ and 15° . The stiffness of the layer ② is sufficiently large and the increasing elastic energy cannot support a fracture penetration into the second layer. The tensile strength of the layer ② is approximately four times that of the layer ① according to Zhou et al. (2018d). The fracture branching is a natural result of the evolution equation of the

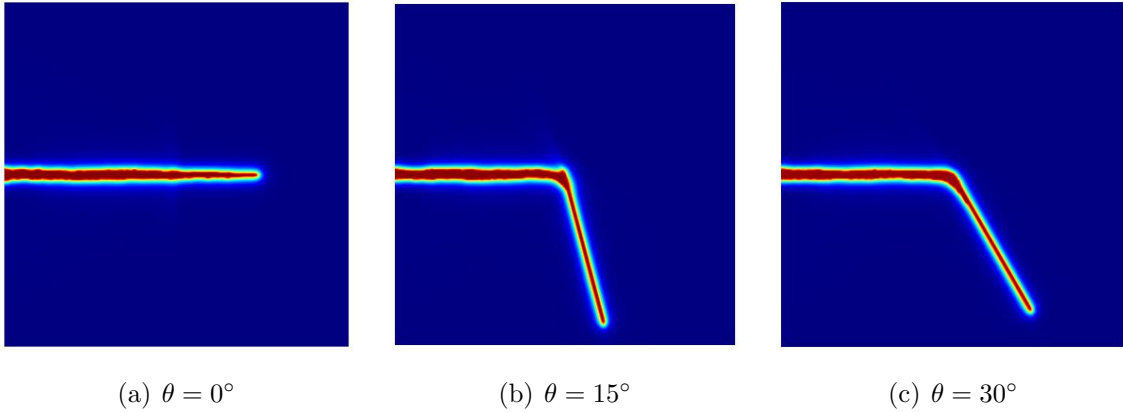


Fig. 7. Fracture propagation patterns for $E_2 = 2E_1$ at $t = 200$ s

phase field after the fracture reaches the layer interface. Given different inclination angles, the time for a fracture propagates to the same distance is relatively different. Therefore, the time point displayed is 100 s in Fig. 8a and 8b and 63.02 s in Fig. 8c.

The branched fractures are symmetrical for $\theta = 0^\circ$ but asymmetric for $\theta = 15^\circ$. The lower fracture is longer than the upper fracture because of the asymmetry of the layer interface along the vertical direction. For the inclination angle $\theta = 30^\circ$, the fracture pattern is similar to that of $E_2 = 2E_1$ in Fig. 7c. Only the singly-deflected scenario is shown and the propagating fracture moves to the bottom boundary while the case of $E_2 = 4E_1$ produces a relatively large fracture propagation velocity. In addition, Figs. 7 and 8 show a narrower fracture after the fracture penetrates or deflects because of unavoidable fluid penetration in the fractures formed at a relatively small fluid pressure level with normal extension of damage.

5.3 Effective maximum stress

In the soft-to-stiff configuration, the effective maximum stress distributions for $E_2 = 2E_1$ and $E_2 = 4E_1$ are displayed in Figs. 9 and 10, respectively. Note that the effective maximum stress in

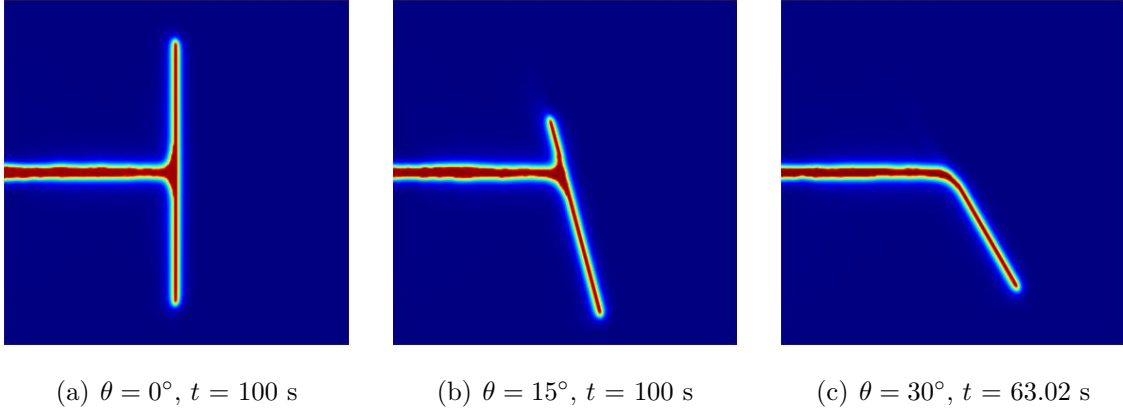


Fig. 8. Fracture propagation patterns for $E_2 = 4E_1$

this study is defined as $\max(\sigma_1, 0)$, with σ_1 being the effective first principal stress. In addition, the region with $\phi \geq 0.95$ is removed from Figs. 9 and 10 to show an improved fracture shape. The stress distributions coincide with the fracture patterns. The stress concentration is observed only around the fracture tip for the penetration and doubly-deflected scenarios. However, stress for the singly-deflected scenario also concentrates in the area where the fracture deflects, except the fracture tip. Note that the stress values in Figs. 9 and 10 are realistic because stress singularity exists at a fracture tip and the stress value theoretically approaches infinity based on linear elastic fracture mechanics. However, the phase field in a PFM smears the sharp fracture. Therefore, the tensile stress value at the fracture tip cannot be infinity. By contrast, this stress decreases as the length scale l_0 increases.

5.4 Displacement field

We also investigate the vertical displacement distributions of the calculation domain for $E_2 = 2E_1$ and $E_2 = 4E_1$ at different time t . In the simulations, the vertical displacement is relatively large around the fracture region and the displacement increases with fracture propagation. We set a

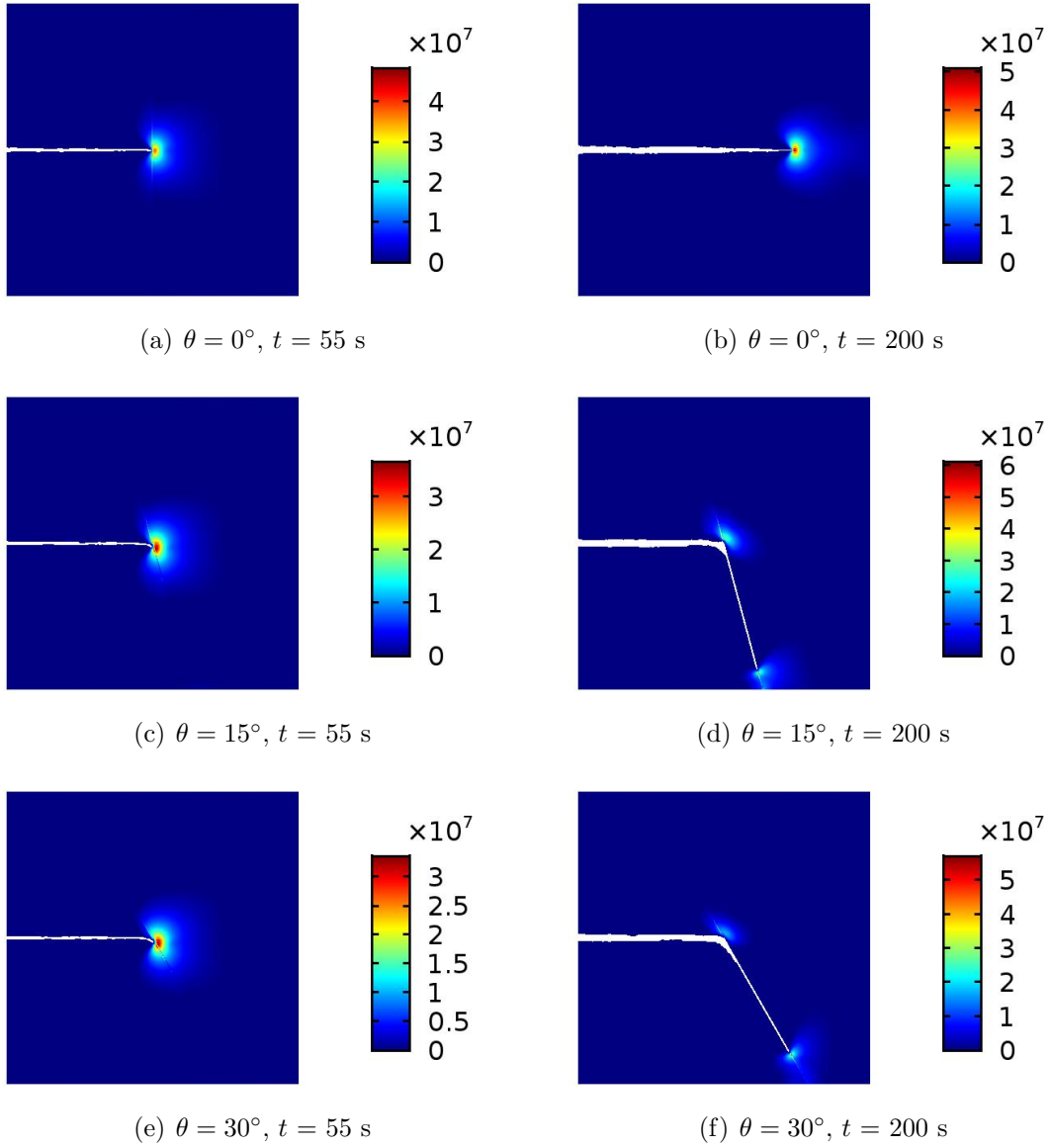


Fig. 9. Effective maximum stress distributions for $E_2 = 2E_1$ (Unit: Pa)

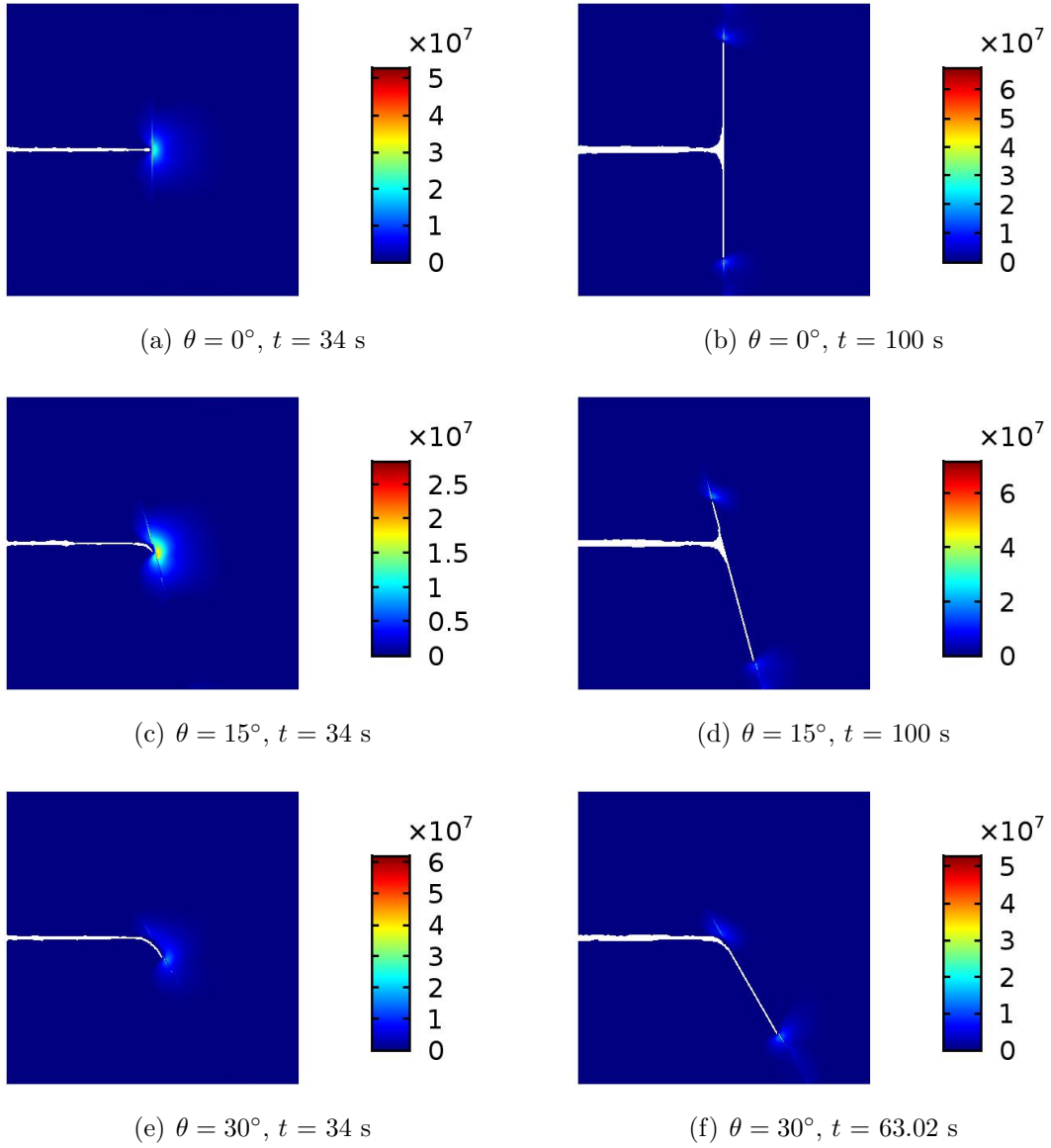


Fig. 10. Effective maximum stress distributions for $E_2 = 4E_1$ (Unit: Pa)

straight monitoring path L1 with its starting point (-2 m, 0.02 m) and ending point (2 m, 0.02 m). That is, the vertical coordinate of the path L1 is identical to that of the upper edge of the pre-existing notch. Figure 11 shows the vertical displacement along path L1 for $E_2 = 2E_1$ and $E_2 = 4E_1$ when the fracture reaches the layer interface. The displacement pattern is similar to those in Mikelic et al. (2013); Zhou et al. (2018c). The vertical displacement decreases along the direction of the fracture propagation, which is consistent with the analytical solution of Sneddon and Lowengrub (1969). In addition, the increase in the inclination angle θ slightly decreases the vertical displacement. The reason is that a larger inclination angle results in a larger stiffer layer volume in the direction normal to the propagating fracture, thereby restricting the upward deformation of the softer layer.

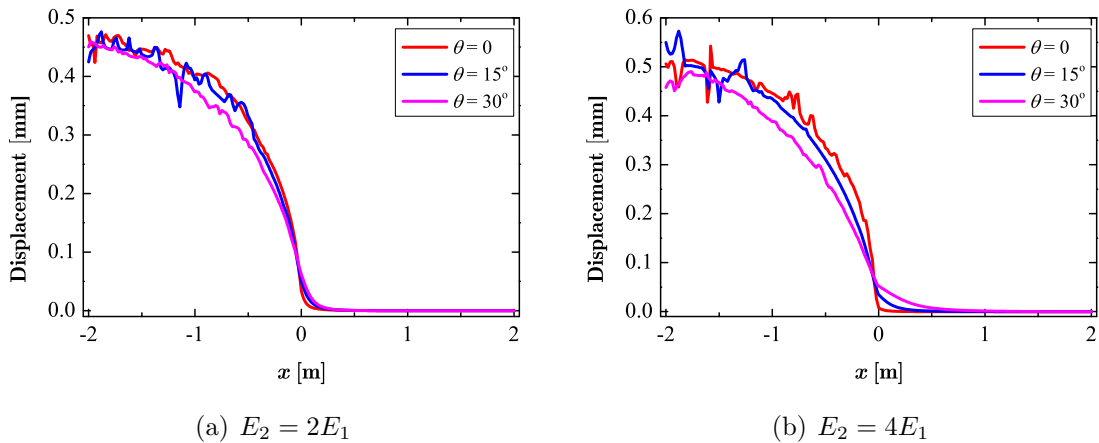


Fig. 11. Vertical displacement along the path L1 when the fracture reaches the layer interface in the soft-to-stiff configuration

Figure 12 shows the maximum vertical displacement on the upper left edge of the domain when the time increases. In the soft-to-stiff configuration, the maximum displacement increases rapidly in the first 50 s ($E_2 = 2E_1$) and 25 s ($E_2 = 4E_1$). Thereafter, the maximum displacement increases at a low rate because the fracture propagation is depressed by the stiffer layer

②. In particular, the inclination angle $\theta = 30^\circ$ achieves a relatively small maximum vertical displacement. Another reason for the second stage with a small increase rate in the vertical displacement is fracture deflection at the layer interface. In addition, slight displacement fluctuation is observed in the XFEM simulation of Vahab et al. (2018).

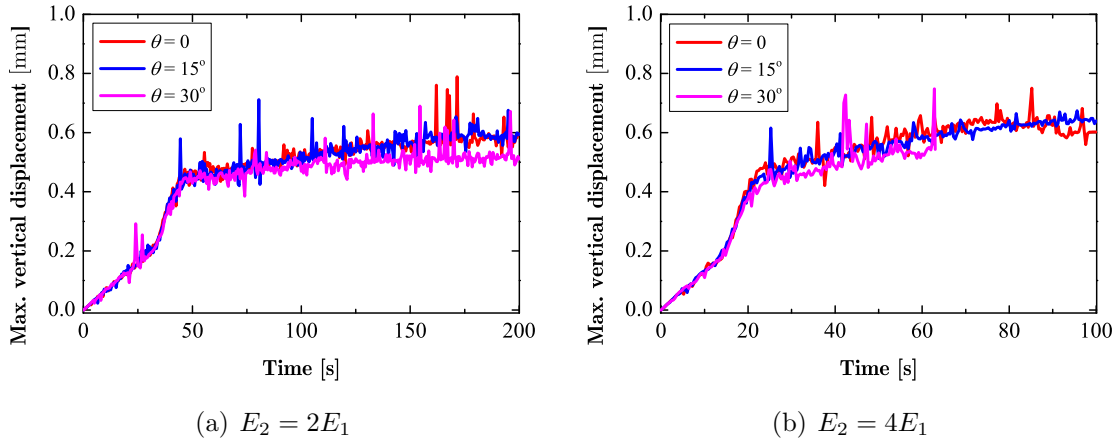


Fig. 12. Maximum vertical displacement along the upper left boundary in the soft-to-stiff configuration

5.5 Fluid pressure

Figures 13 and 14 show the fluid pressure field for $E_2 = 2E_1$ and $E_2 = 4E_1$. The fluid pressure field is consistent with the phase field while the maximum pressure appears in the hydraulic fractures. Figure 15 shows the fluid pressure with the increasing time. The data is picked at the point (-2 m, 0). The fluid pressure has a similar trend with the maximum vertical displacement in Fig. 12. Note that the fluid pressure increases rapidly in the first 40 s ($E_2 = 2E_1$) and 20 s ($E_2 = 4E_1$). Thereafter, the increasing rate of the fluid pressure decreases. When $\theta = 0^\circ$ and 30° , the fluid pressure-time curves are similar. However, the inclination angle $\theta = 30^\circ$ obtains a relatively low fluid pressure. The pattern of fluid pressure mainly results from the fracture

pattern, soft-to-stiff setting, and relatively low porosity used in the simulation.

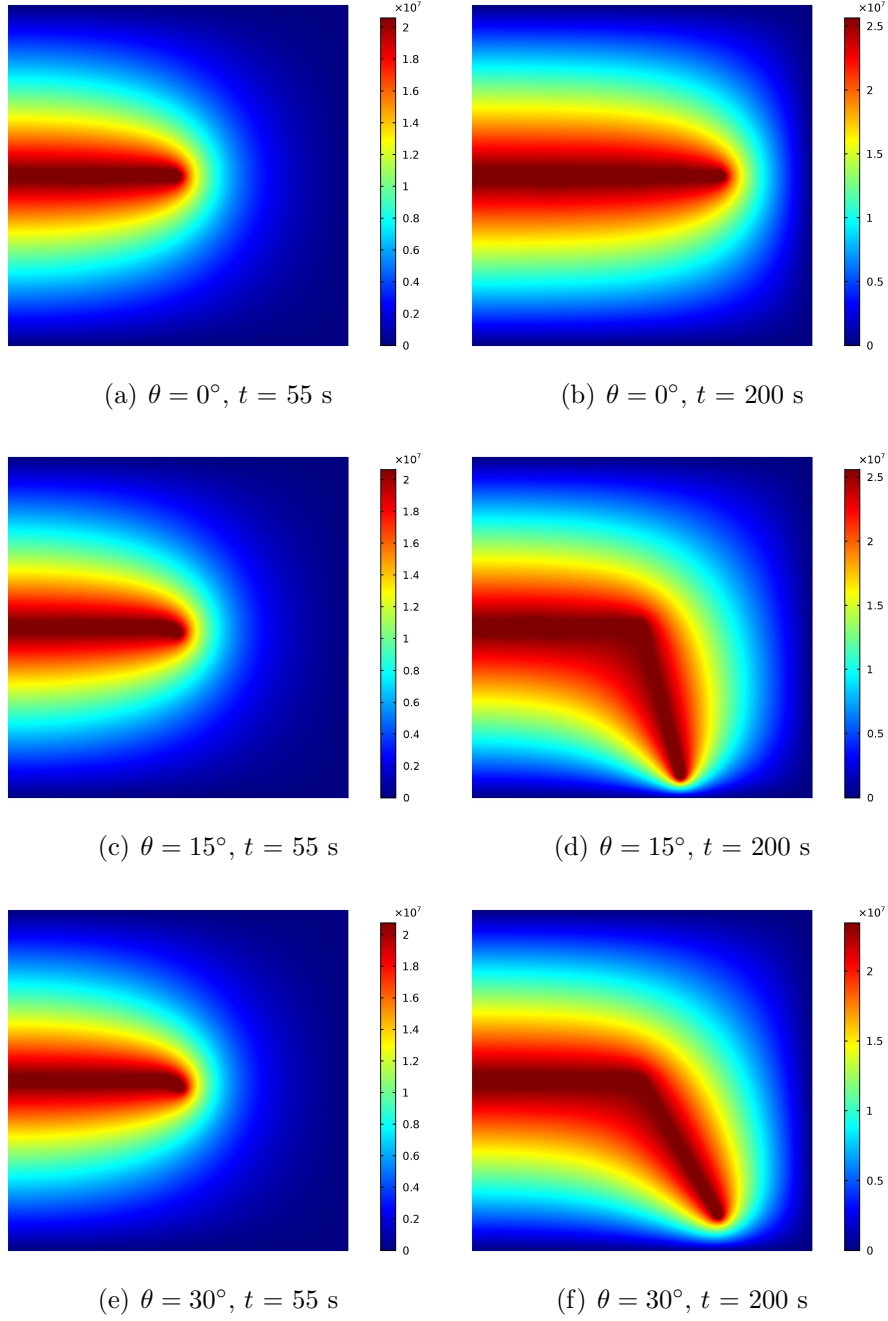


Fig. 13. Fluid pressure distributions for $E_2 = 2E_1$ (Unit: Pa)

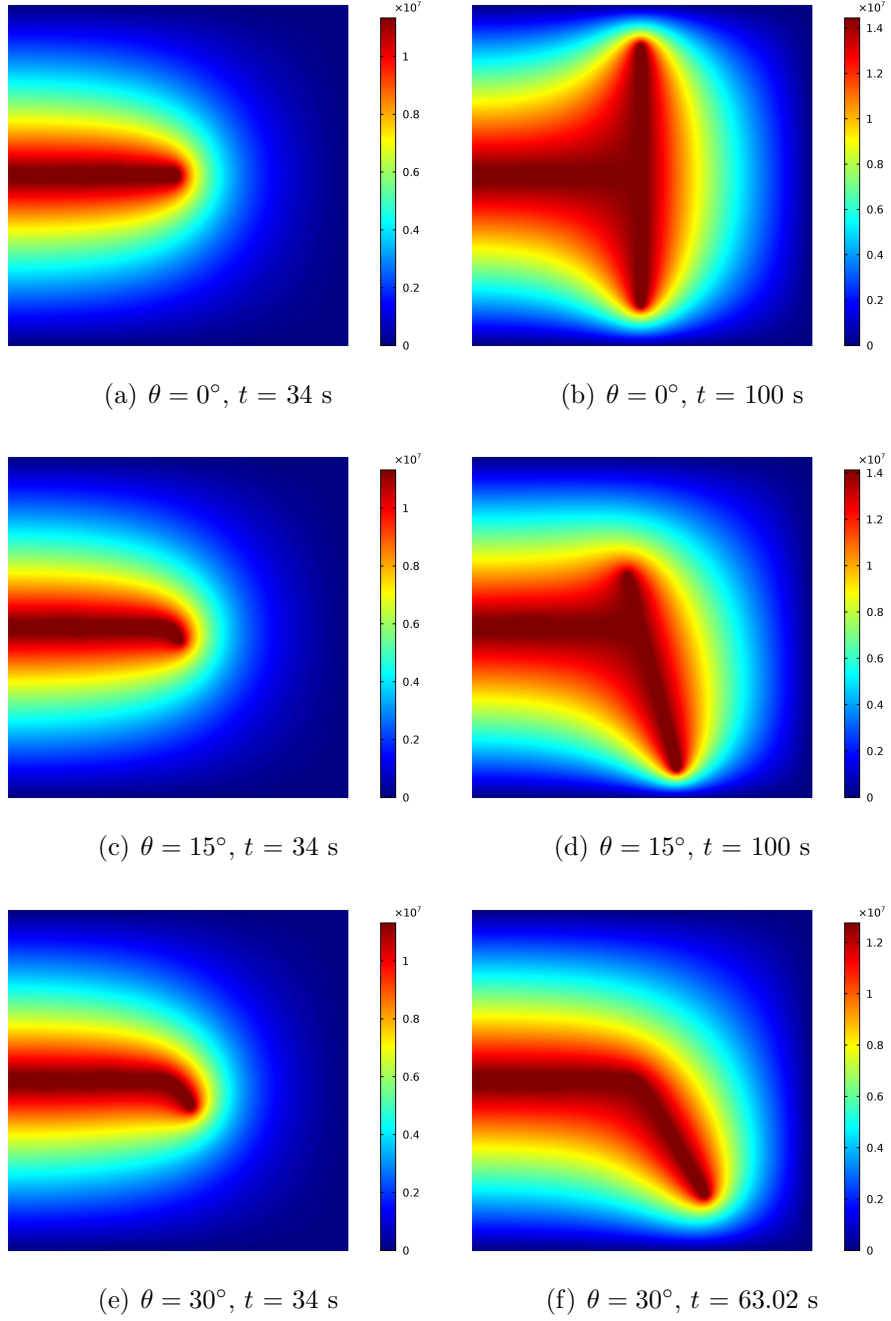


Fig. 14. Fluid pressure distributions for $E_2 = 4E_1$ (Unit: Pa)

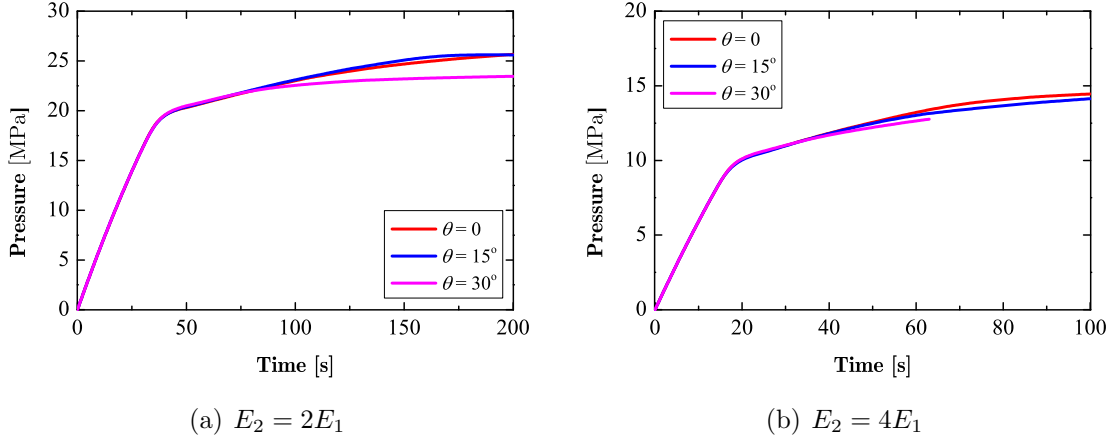


Fig. 15. Fluid pressure in the pre-existing notch in the soft-to-stiff configuration

6 Stiff-to-soft configuration

6.1 Fracture pattern

This section presents the numerical results for the stiff-to-soft configuration ($E_1 = 2E_2$ and $E_1 = 3E_2$). Figures 16 and 17 represent the hydraulic fracture patterns for $E_1 = 2E_2$ and $E_1 = 3E_2$ at different time t , respectively. Only the penetration scenario is obtained in the stiff-to-soft configuration, which is different from the observations in the soft-to-stiff configuration. Singly-deflected, doubly-deflected, and penetration scenarios can be all simulated in the soft-to-stiff configuration. The fracture penetration scenario in the stiff-to-soft configuration is a natural result calculated from the evolution equation of the phase field, and the fracture penetration pattern is formed because the softer layer ② has a lower tensile strength than the stiffer layer ① according to Zhou et al. (2018d).

Figures 16 and 17 also show that the fracture width increases when the fracture penetrates into the softer layer ②. By comparing Figs. 16 and 17, it is observed that the fracture in the layer ② has a larger width when the stiffness of the layer ② is smaller. The inclination angle

also influences the fracture pattern. When $\theta = 0$, the fractures in the layers ① and ② propagate horizontally. However, when $\theta = 15^\circ$ and 30° , the hydraulic fracture deflects slightly after it crosses the layer interface. The hydraulic fracture in the layer ② intersects the fracture in the layer ① at a small angle, which increases slightly as θ increases.

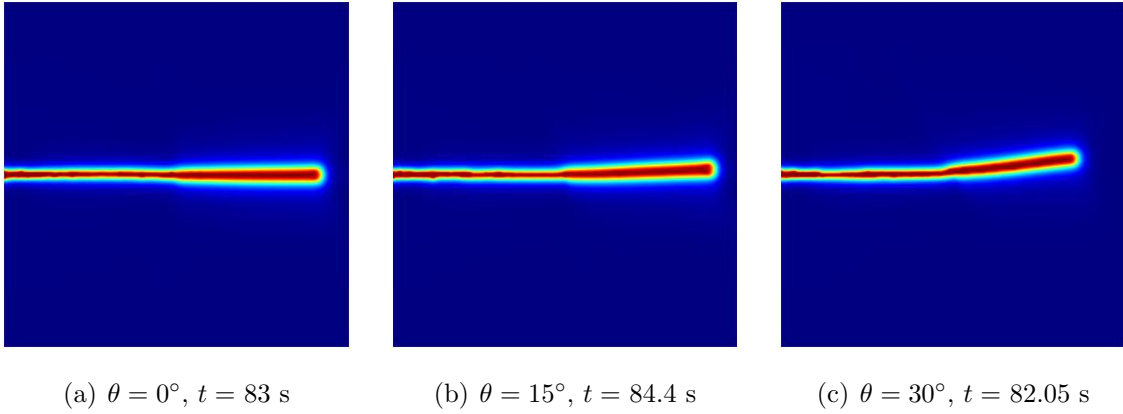


Fig. 16. Fracture propagation patterns for $E_1 = 2E_2$

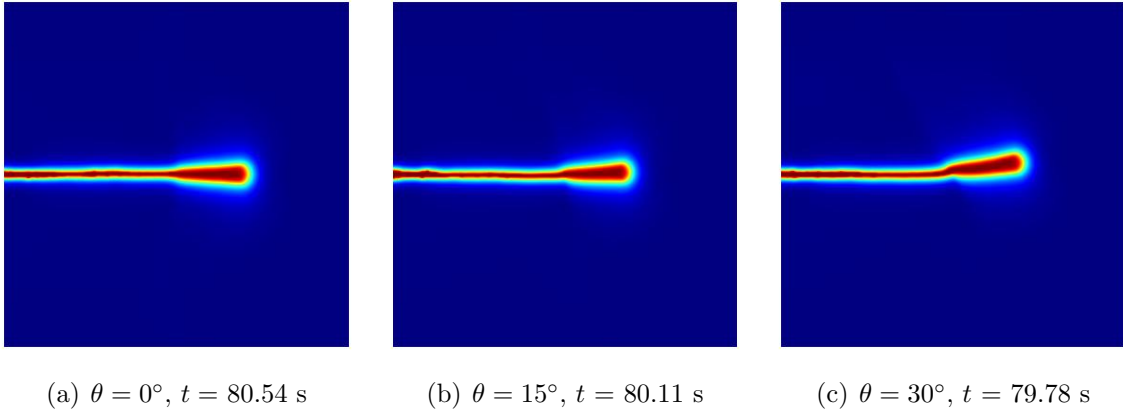


Fig. 17. Fracture propagation patterns for $E_1 = 3E_1$

6.2 Effective maximum stress

In the stiff to soft configuration, the effective maximum stress distributions for $E_1 = 2E_2$ and $E_1 = 3E_2$ at different time t are shown in Figs. 18 and 19, respectively. The stress distributions

coincide with the fracture patterns. The stress concentration is observed only around the fracture tip owing to the penetration scenario. In addition, the effective maximum stress around the fracture tip decreases when the hydraulic fracture propagates into the layer ②. The difference between the stress in the two layers ① and ② reflects again the difference in the tensile strength for resisting fracturing.

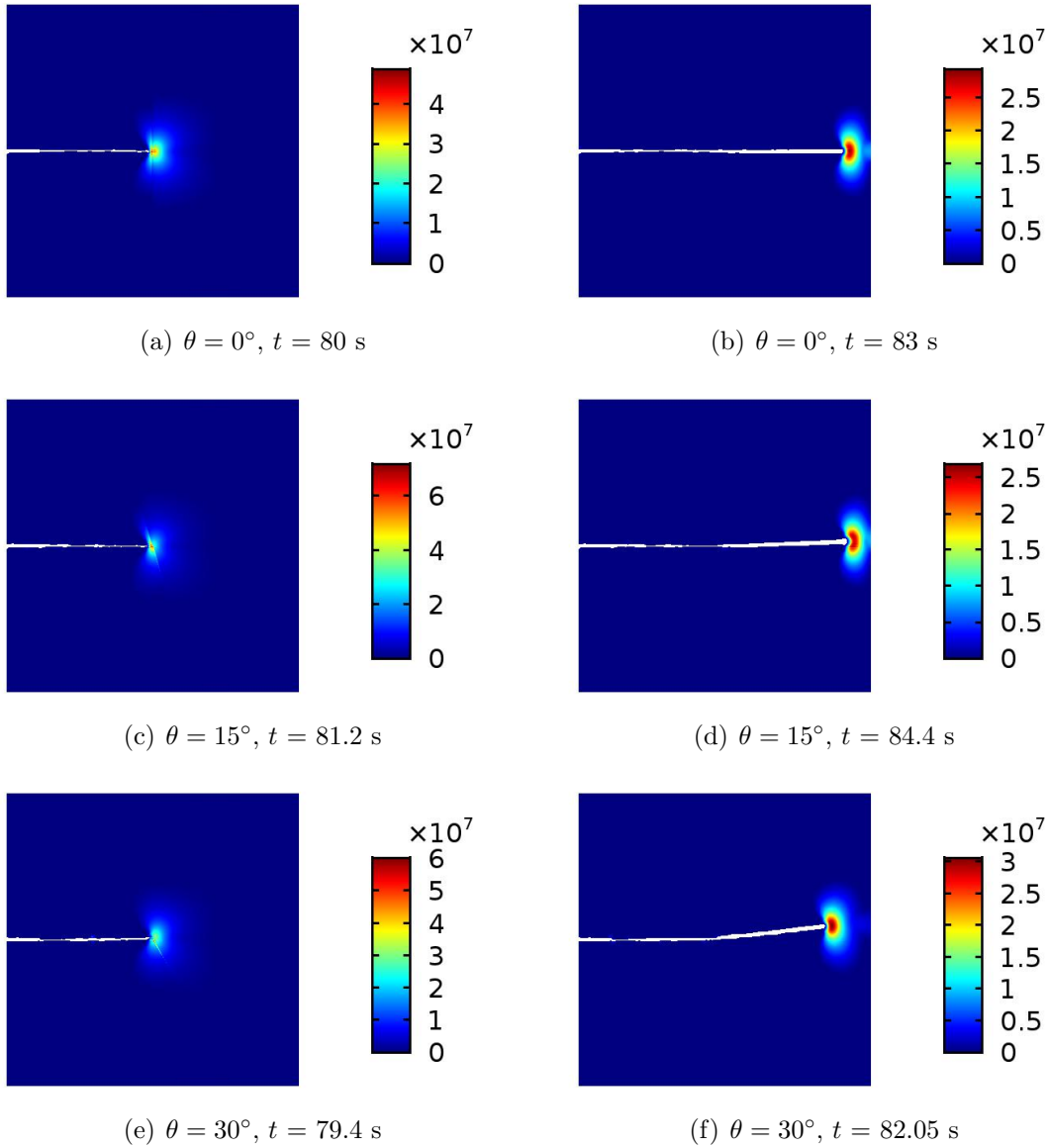


Fig. 18. Effective maximum stress distributions for $E_1 = 2E_2$ (Unit: Pa)

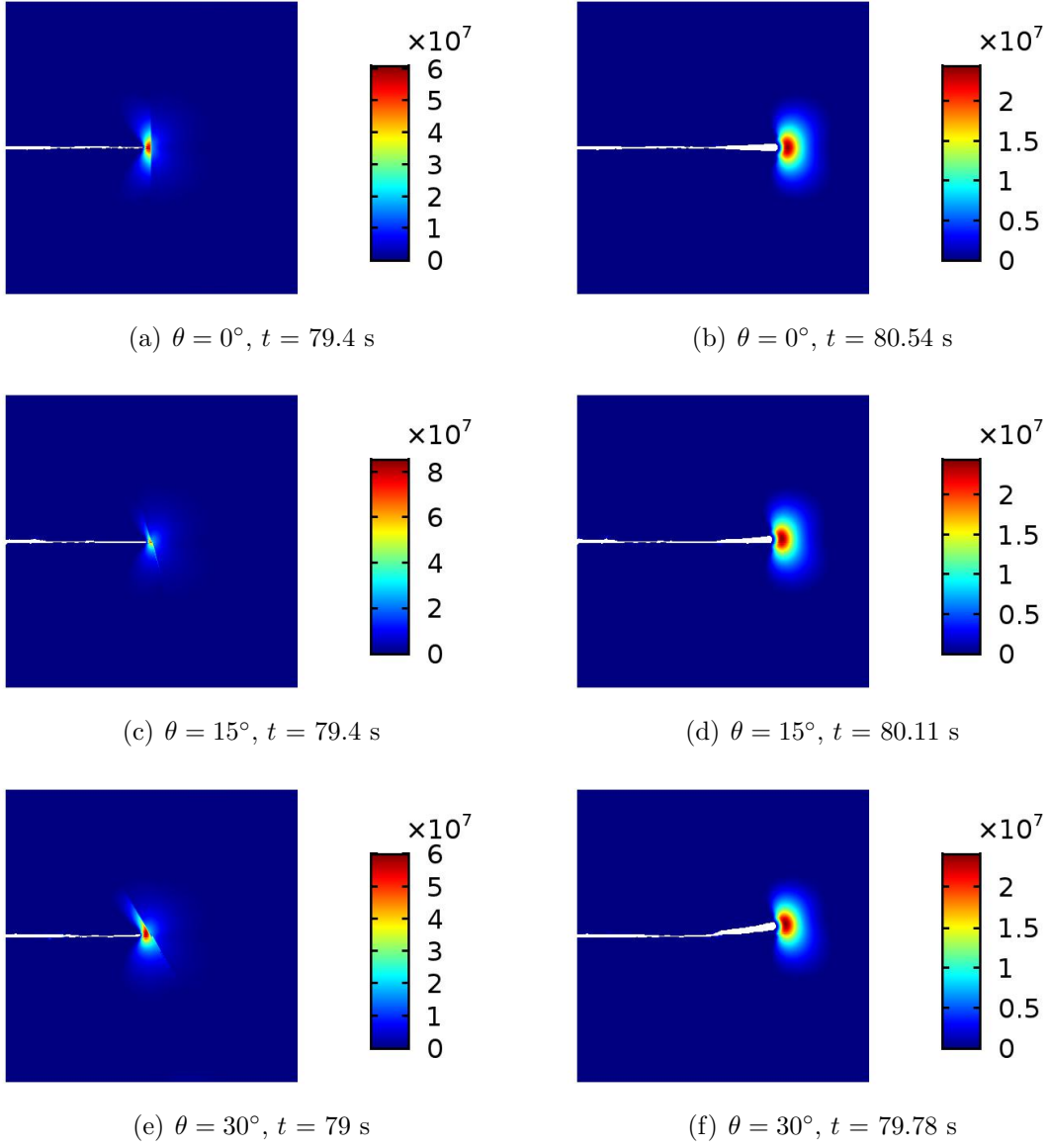


Fig. 19. Effective maximum stress distributions for $E_1 = 3E_2$ (Unit: Pa)

6.3 Displacement field

The vertical displacement distributions of the calculation domain for $E_1 = 2E_2$ and $E_1 = 3E_2$ at different time t is investigated. When hydraulic fracture propagates in the stiffer layer ①, the maximum vertical displacement occurs around the fluid injection region and the displacement increases along with the fracture propagation. However, increasing vertical displacement exists around the fracture domain in the softer layer ② when the hydraulic fracture penetrates deep into the layer ②.

Figure 20 shows the vertical displacement along the path L1 for $E_1 = 2E_2$ and $E_1 = 3E_2$ when the fracture reaches the layer interface. The displacement pattern is similar to those in the soft to stiff configuration. The vertical displacement decreases along the direction of fracture propagation while the displacement increases slightly as the inclination angle θ increases.

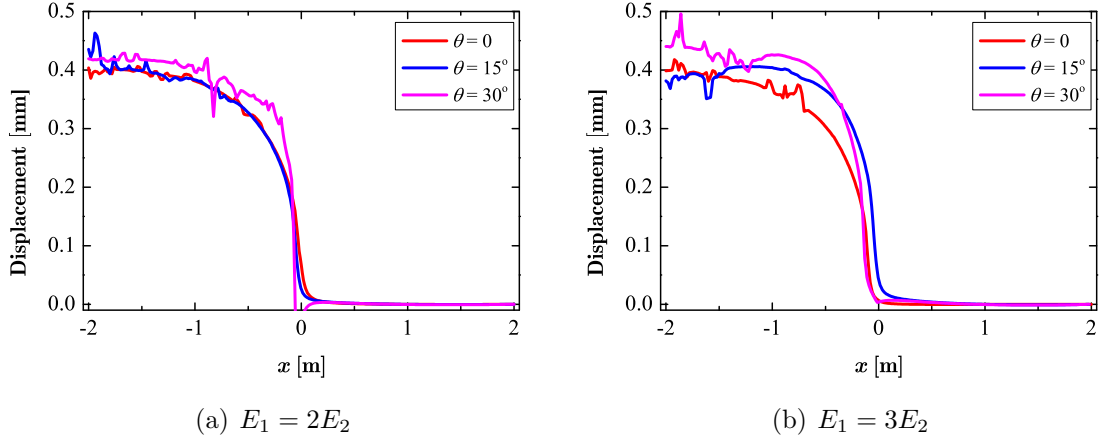


Fig. 20. Vertical displacement along the path L1 when the fracture reaches the layer interface in the stiff-to-soft configuration

Figure 21 shows the maximum vertical displacement on the upper left edge when time increases in the stiff-to-soft configuration. As shown in Fig. 21, the maximum displacement increases at a relative small rate in the first 65 s. Thereafter, when the hydraulic fracture

reaches the layer interface and propagates deep into the layer ②, the maximum displacement increases at a relatively large rate. In addition, the curves of the maximum displacement versus time are minimally affected by the inclination angle θ .

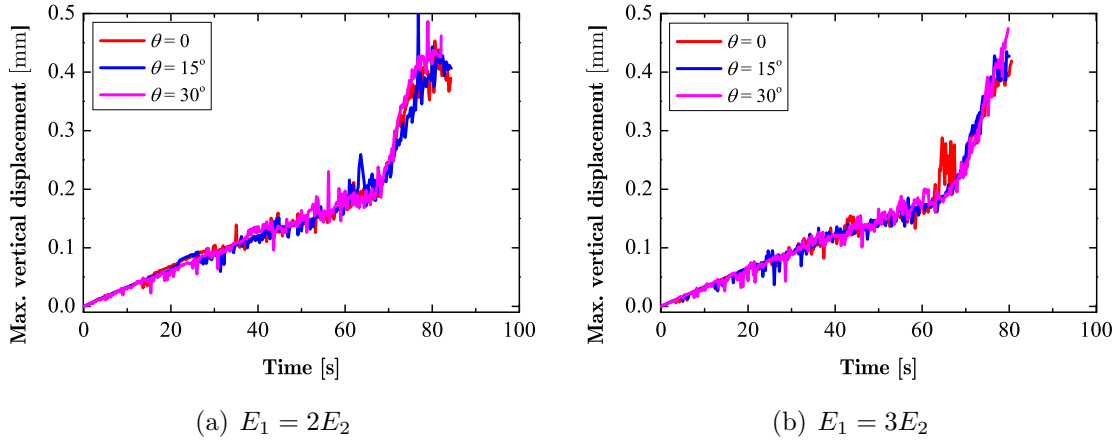


Fig. 21. Maximum vertical displacement along the upper left boundary in the stiff-to-soft configuration

6.4 Fluid pressure

Figure 22 shows the fluid pressure when the time increases in the stiff-to-soft configuration. The data is also picked at the point $(-2 \text{ m}, 0)$. The fluid pressure has a similar trend to that in the soft-to-stiff configuration in Fig. 15. The fluid pressure increases rapidly in the first 65 s. Thereafter, the increasing rate of the fluid pressure decreases and the pressure is nearly stable. Furthermore, for the stiff-to-soft configuration, the second stage is observed to be considerably shorter than the soft-to-stiff configuration. The inclination angle θ has minimal effect on the fluid pressure-time curve.

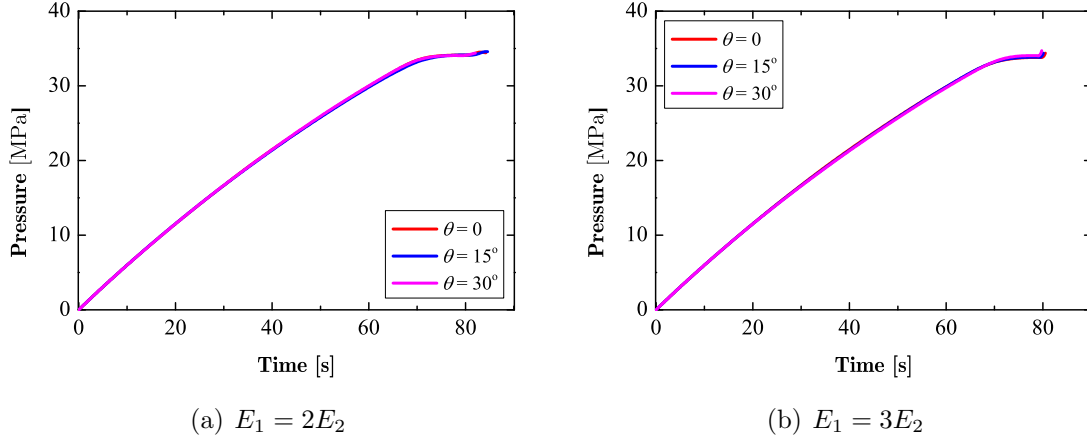


Fig. 22. Fluid pressure in the pre-existing notch in the stiff-to-soft configuration

6.5 Guidance for HF practice

Figure 23 summarizes all the fracture patterns at the layer interface for different E_2/E_1 , inclination angle θ , and the data in a single porous layer (Zhou et al., 2018c) ($E_2 = E_1$). On the basis of the relationship between E_2/E_1 and θ , three regions formed in this figure represent the three fracture patterns—penetration, singly-deflected, and doubly-deflected scenarios. Note that a low E_2/E_1 or a medium E_2/E_1 with a low θ produces the penetration scenario. A high θ with a medium or high E_2/E_1 corresponds to the singly-deflected scenario, while only a high E_2/E_1 with a low θ will form the doubly-deflected scenario. Therefore, the phase field model and numerical investigation in this research can easily reflect the influence of layer stiffness and interface angle on fracture patterns. In addition, the summary figure, which will be further improved by using PFM in future studies, can be applied for unconventional HF in shale gas development and to study safety and environmental concerns and efficiency issues in current HF practices. For example, if the elastic parameters of two neighboring layers are known, then the perforation direction in HF can be optimized according to Fig. 23 to avoid fracture penetration into the neighboring layer due to the potential risks for water contamination and stability of the

geological system.

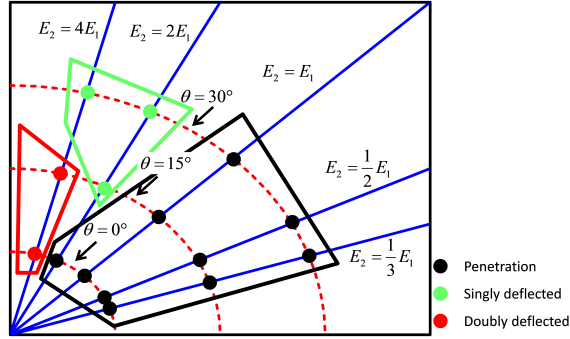


Fig. 23. Summation of fracture patterns for different E_2/E_1 and interface angle θ

7 Conclusions

This study applies a phase field framework to examine hydraulic fracture growth in naturally layered geological formations. The total energy functional used fully includes the influence of fluid pressure, and the fracture pattern is the natural result of minimization of the energy functional. In addition, we consider the soft-to-stiff and the stiff-to-soft configurations where the layer interface exhibits different inclination angles. Therefore, the relationship between the phase field (fracture pattern) and the stiffness contrast and inclination angle of the geological formations, is revealed. The numerical investigation in this study supports the following:

(1) The huge advantage of the phase field framework over the X-FEM framework lies in the fact that penetration criteria are also not required when hydraulic fractures reach the material interfaces. In addition, the phase field implementation does not require tracking the fracture paths algorithmically.

(2) Penetration, singly-deflected, and doubly-deflected fracture scenarios can be predicted using PFM. In the soft-to-stiff configuration, the simulations exhibit penetration or symmetrical

doubly-deflected scenarios when the pre-existing fracture is perpendicular to the layer interface. When the interface angle is 15° , singly-deflected or asymmetric doubly-deflected scenarios are obtained. Only the singly-deflected scenario is obtained for the interface angle of 30° .

(3) In the stiff-to-soft configuration, only the penetration scenario is obtained with widening fractures when the hydraulic fractures penetrate into the softer layer. The fracture in the softer layer deflects at a small angle with the fracture in the stiffer layer and the angle increases as the layer interface angle increases.

Note that our study includes a perfect bonding at the layer interface, which is not always the case in geological settings (Cooke and Underwood, 2001; Xing et al., 2018). Therefore, in future studies, layer interfaces with weak bonding and methods on fixing the interface parameters from the neighboring layers should be involved in the PFM on fracture propagation in layered formations. Laboratory experiments on fractures along weakly-bonded interfaces (Xing et al., 2018) will also be used for further validation of PFM. Another limitation of PFM is that the direct coupling of the permeability and crack opening is difficult to apply because of the smeared representation of fracture. In this sense, future PFMs should introduce substantially accurate permeability models for fractured porous domains.

Acknowledgment

The authors gratefully acknowledge the financial support provided by the Natural Science Foundation of China (51474157), and the RISE-project BESTOFRAF (734370).

References

- Areias, P., Msekh, M., and Rabczuk, T. (2016). Damage and fracture algorithm using the screened poisson equation and local remeshing. *Engineering Fracture Mechanics*, 158:116–143.
- Behnia, M., Goshtasbi, K., Marji, M. F., and Golshani, A. (2014). Numerical simulation of crack propagation in layered formations. *Arabian Journal of Geosciences*, 7(7):2729–2737.
- Belytschko, T. and Lin, J. I. (1987). A three-dimensional impact-penetration algorithm with erosion. *International Journal of Impact Engineering*, 5(1-4):111–127.
- Biot, M. A., Medlin, W., Masse, L., et al. (1983). Fracture penetration through an interface. *Society of Petroleum Engineers Journal*, 23(06):857–869.
- Borden, M. J., Verhoosel, C. V., Scott, M. A., Hughes, T. J., and Landis, C. M. (2012). A phase-field description of dynamic brittle fracture. *Computer Methods in Applied Mechanics and Engineering*, 217:77–95.
- Bourdin, B., Chukwudozie, C. P., Yoshioka, K., et al. (2012). A variational approach to the numerical simulation of hydraulic fracturing. In *SPE Annual Technical Conference and Exhibition*. Society of Petroleum Engineers.
- Bourdin, B., Francfort, G. A., and Marigo, J.-J. (2000). Numerical experiments in revisited brittle fracture. *Journal of the Mechanics and Physics of Solids*, 48(4):797–826.
- Cooke, M. L. and Underwood, C. A. (2001). Fracture termination and step-over at bedding

- interfaces due to frictional slip and interface opening. *Journal of Structural Geology*, 23(2-3):223–238.
- Cui, Z.-D., Liu, D.-A., Zeng, R.-S., Niu, J.-R., Wang, H.-J., and Shi, X.-S. (2013). Resistance of caprock to hydraulic fracturing due to co2 injection into sand lens reservoirs. *Engineering geology*, 164:146–154.
- Dahi-Taleghani, A., Olson, J. E., et al. (2011). Numerical modeling of multistranded-hydraulic-fracture propagation: Accounting for the interaction between induced and natural fractures. *SPE journal*, 16(03):575–581.
- Detournay, E. (2016). Mechanics of hydraulic fractures. *Annual Review of Fluid Mechanics*, 48:311–339.
- Dyskin, A. and Caballero, A. (2009). Orthogonal crack approaching an interface. *Engineering Fracture Mechanics*, 76(16):2476–2485.
- Figueiredo, B., Tsang, C.-F., Rutqvist, J., and Niemi, A. (2017). The effects of nearby fractures on hydraulically induced fracture propagation and permeability changes. *Engineering Geology*, 228:197–213.
- Francfort, G. A. and Marigo, J.-J. (1998). Revisiting brittle fracture as an energy minimization problem. *Journal of the Mechanics and Physics of Solids*, 46(8):1319–1342.
- Gu, H. and Siebrits, E. (2006). Effect of formation modulus contrast on hydraulic fracture height containment. *SPE*, 103822.

- Gudmundsson, A. and Brenner, S. L. (2001). How hydrofractures become arrested. *Terra Nova*, 13(6):456–462.
- Guo, G. and Fall, M. (2018). Modelling of dilatancy-controlled gas flow in saturated bentonite with double porosity and double effective stress concepts. *Engineering Geology*, 243:253–271.
- Jeanpert, J., Iseppi, M., Adler, P., Genthon, P., Sevin, B., Thovert, J.-F., Dewandel, B., and Join, J.-L. (2019). Fracture controlled permeability of ultramafic basement aquifers. inferences from the koniambo massif, new caledonia. *Engineering Geology*, 256:67–83.
- Khoei, A., Hirmand, M., Vahab, M., and Bazargan, M. (2015). An enriched fem technique for modeling hydraulically driven cohesive fracture propagation in impermeable media with frictional natural faults: Numerical and experimental investigations. *International Journal for Numerical Methods in Engineering*, 104(6):439–468.
- Kim, W.-Y. (2013). Induced seismicity associated with fluid injection into a deep well in youngstown, ohio. *Journal of Geophysical Research: Solid Earth*, 118(7):3506–3518.
- Lee, S., Wheeler, M. F., and Wick, T. (2016). Pressure and fluid-driven fracture propagation in porous media using an adaptive finite element phase field model. *Computer Methods in Applied Mechanics and Engineering*, 305:111–132.
- Lee, S., Wheeler, M. F., and Wick, T. (2017a). Iterative coupling of flow, geomechanics and adaptive phase-field fracture including level-set crack width approaches. *Journal of Computational and Applied Mathematics*, 314:40–60.
- Lee, S., Wheeler, M. F., Wick, T., and Srinivasan, S. (2017b). Initialization of phase-field

- fracture propagation in porous media using probability maps of fracture networks. *Mechanics Research Communications*, 80:16–23.
- Lei, Q., Latham, J.-P., Xiang, J., and Tsang, C.-F. (2017). Role of natural fractures in damage evolution around tunnel excavation in fractured rocks. *Engineering Geology*, 231:100–113.
- Li, Y., Chen, Y.-F., and Zhou, C.-B. (2014). Hydraulic properties of partially saturated rock fractures subjected to mechanical loading. *Engineering geology*, 179:24–31.
- Liu, J., Ding, W., Gu, Y., Xiao, Z., Dai, J., Dai, P., Chen, X., and Zhao, G. (2018). Methodology for predicting reservoir breakdown pressure and fracture opening pressure in low-permeability reservoirs based on an in situ stress simulation. *Engineering Geology*, 246:222–232.
- Liu, K. and Sheng, J. J. (2019). Experimental study of the effect of stress anisotropy on fracture propagation in eagle ford shale under water imbibition. *Engineering Geology*, 249:13–22.
- Liu, Y., Li, H., Luo, C., and Wang, X. (2014). In situ stress measurements by hydraulic fracturing in the western route of south to north water transfer project in china. *Engineering Geology*, 168:114–119.
- Miehe, C., Hofacker, M., and Welschinger, F. (2010a). A phase field model for rate-independent crack propagation: Robust algorithmic implementation based on operator splits. *Computer Methods in Applied Mechanics and Engineering*, 199(45):2765–2778.
- Miehe, C. and Mauthe, S. (2016). Phase field modeling of fracture in multi-physics problems. part iii. crack driving forces in hydro-poro-elasticity and hydraulic fracturing of fluid-saturated porous media. *Computer Methods in Applied Mechanics and Engineering*, 304:619–655.

- Miehe, C., Welschinger, F., and Hofacker, M. (2010b). Thermodynamically consistent phase-field models of fracture: Variational principles and multi-field fe implementations. *International Journal for Numerical Methods in Engineering*, 83(10):1273–1311.
- Mikelic, A., Wheeler, M. F., and Wick, T. (2013). A phase field approach to the fluid filled fracture surrounded by a poroelastic medium. *ICES report*, 1315.
- Mikelić, A., Wheeler, M. F., and Wick, T. (2015a). Phase-field modeling of a fluid-driven fracture in a poroelastic medium. *Computational Geosciences*, 19(6):1171–1195.
- Mikelić, A., Wheeler, M. F., and Wick, T. (2015b). A quasi-static phase-field approach to pressurized fractures. *Nonlinearity*, 28(5):1371.
- Moës, N. and Belytschko, T. (2002). Extended finite element method for cohesive crack growth. *Engineering fracture mechanics*, 69(7):813–833.
- Nguyen, O., Repetto, E., Ortiz, M., and Radovitzky, R. (2001). A cohesive model of fatigue crack growth. *International Journal of Fracture*, 110(4):351–369.
- Peerlings, R., De Borst, R., Brekelmans, W., De Vree, J., and Spee, I. (1996). Some observations on localisation in non-local and gradient damage models. *European Journal of Mechanics A: Solids*, 15(6):937–953.
- Pudasaini, S. P. (2016). A novel description of fluid flow in porous and debris materials. *Engineering Geology*, 202:62–73.
- Rabczuk, T., Zi, G., Bordas, S., and Nguyen-Xuan, H. (2010). A simple and robust three-

- dimensional cracking-particle method without enrichment. *Computer Methods in Applied Mechanics and Engineering*, 199(37):2437–2455.
- Rabczuk, T., Zi, G., Gerstenberger, A., and Wall, W. A. (2008). A new crack tip element for the phantom-node method with arbitrary cohesive cracks. *International Journal for Numerical Methods in Engineering*, 75(5):577–599.
- Ren, F., Ma, G., Fan, L., Wang, Y., and Zhu, H. (2017a). Equivalent discrete fracture networks for modelling fluid flow in highly fractured rock mass. *Engineering Geology*, 229:21–30.
- Ren, H., Zhuang, X., Cai, Y., and Rabczuk, T. (2016). Dual-horizon peridynamics. *International Journal for Numerical Methods in Engineering*, 108(12):1451–1476.
- Ren, H., Zhuang, X., and Rabczuk, T. (2017b). Dual-horizon peridynamics: A stable solution to varying horizons. *Computer Methods in Applied Mechanics and Engineering*, 318:762–782.
- Santillán, D., Juanes, R., and Cueto-Felgueroso, L. (2017). Phase field model of fluid-driven fracture in elastic media: Immersed-fracture formulation and validation with analytical solutions. *Journal of Geophysical Research: Solid Earth*, 122(4):2565–2589.
- Segall, P. and Fitzgerald, S. D. (1998). A note on induced stress changes in hydrocarbon and geothermal reservoirs. *Tectonophysics*, 289(1-3):117–128.
- Smith, M., Bale, A., Britt, L., Klein, H., Siebrits, E., and Dang, X. (2001). Layered modulus effects on fracture propagation, proppant placement and fracture modelling. *SPE journal*, 71654.

- Sneddon, I. N. and Lowengrub, M. (1969). *Crack problems in the classical theory of elasticity*.
John Wiley & Sons.
- Vahab, M., Akhondzadeh, S., Khoei, A., and Khalili, N. (2018). An x-fem investigation of hydrofracture evolution in naturally-layered domains. *Engineering Fracture Mechanics*, 191:187–204.
- Van Eekelen, H. et al. (1982). Hydraulic fracture geometry: fracture containment in layered formations. *Society of Petroleum Engineers Journal*, 22(03):341–349.
- Wang, H. (2015). Numerical modeling of non-planar hydraulic fracture propagation in brittle and ductile rocks using xfem with cohesive zone method. *Journal of Petroleum Science and Engineering*, 135:127–140.
- Wheeler, M., Wick, T., and Wollner, W. (2014). An augmented-lagrangian method for the phase-field approach for pressurized fractures. *Computer Methods in Applied Mechanics and Engineering*, 271:69–85.
- Xing, P., Yoshioka, K., Adachi, J., El-Fayoumi, A., and Bungler, A. P. (2018). Laboratory demonstration of hydraulic fracture height growth across weak discontinuities. *Geophysics*, 83(2):MR93–MR105.
- Zhang, Z. and Ghassemi, A. (2011). Simulation of hydraulic fracture propagation near a natural fracture using virtual multidimensional internal bonds. *International Journal for Numerical and Analytical Methods in Geomechanics*, 35(4):480–495.
- Zhou, C.-B., Zhao, X.-J., Chen, Y.-F., Liao, Z., and Liu, M.-M. (2018a). Interpretation of high pressure pack tests for design of impervious barriers under high-head conditions. *Engineering Geology*, 234:112–121.

- Zhou, S., Rabczuk, T., and Zhuang, X. (2018b). Phase field modeling of quasi-static and dynamic crack propagation: Comsol implementation and case studies. *Advances in Engineering Software*, 122:31–49.
- Zhou, S., Zhuang, X., and Rabczuk, T. (2018c). A phase-field modeling approach of fracture propagation in poroelastic media. *Engineering Geology*, 240:189–203.
- Zhou, S., Zhuang, X., and Rabczuk, T. (2019a). Phase field modeling of brittle compressive-shear fractures in rock-like materials: A new driving force and a hybrid formulation. *Computer Methods in Applied Mechanics and Engineering*, 355:729–752.
- Zhou, S., Zhuang, X., and Rabczuk, T. (2019b). Phase-field modeling of fluid-driven dynamic cracking in porous media. *Computer Methods in Applied Mechanics and Engineering*, 350:169–198.
- Zhou, S., Zhuang, X., Zhu, H., and Rabczuk, T. (2018d). Phase field modelling of crack propagation, branching and coalescence in rocks. *Theoretical and Applied Fracture Mechanics*, 96:174–192.
- Zhuang, X., Augarde, C., and Mathisen, K. (2012). Fracture modeling using meshless methods and level sets in 3d: framework and modeling. *International Journal for Numerical Methods in Engineering*, 92(11):969–998.
- Zhuang, X., Zhu, H., and Augarde, C. (2014). An improved meshless shepard and least squares method possessing the delta property and requiring no singular weight function. *Computational Mechanics*, 53(2):343–357.